J. Fluid Mech. (2022), *vol*. 951, A2, doi:10.1017/jfm.2022.826

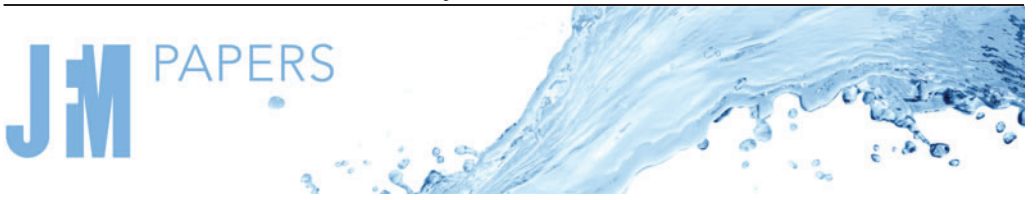

A spectral inspection for turbulence amplification in oblique shock wave/turbulent boundary layer interaction

Ming Yu[1,2], **MingXiang Zhao**[2,3], **ZhiGong Tang**[1], **XianXu Yuan**[1,†] and **ChunXiao Xu**[2,†]

[1]State Key Laboratory of Aerodynamics, Mianyang 621000, PR China

[2]Key Laboratory of Applied Mechanics, Ministry of Education, Institute of Fluid Mechanics, Department of Engineering Mechanics, Tsinghua University, Beijing 100084, PR China

[3]Beijing Institute of Space Launch Technology, Beijing 100076, PR China

(Received 11 April 2022; revised 7 August 2022; accepted 23 September 2022)

Turbulence amplification and the large-scale coherent structures in shock wave/turbulent boundary layer interaction flows have been studied at length in previous research, while the direct association between these two flow features is still lacking. In the present study, the transport equation of turbulent kinetic energy spectra is derived and utilized to analyse the scale-by-scale energy budget across the interaction zone, enabling us to reveal the association between the genesis of the large-scale motions and the turbulence amplification. For the presently considered flow with incipient shock-induced separation, we identified in turbulent kinetic energy spectra distribution that the most energetic motions are converted from the near-wall small-scale motions to large-scale motions consisting of velocity streaks and cross-stream circulations as they go through the interaction zone. The amplification of streamwise velocity fluctuation is triggered first, resulting in the emergence of large-scale velocity streaks, which is attributed to the adverse pressure gradient, as indicated by the spectra of the production term. The energy carried by large-scale velocity streaks is transferred to other velocity components by the pressure-strain term, producing large-scale cross-stream circulations. When large-scale motions are convected downstream, their energy is transferred via turbulent cascade to smaller scales and dissipated by viscosity. The spanwise uniform fluctuations, reminiscent of the unsteadiness of the separation bubble, are contributed primarily by the inter-scale energy transfer from the finite spanwise scale motions.

Key words: high-speed flow, compressible turbulence, turbulent boundary layers

† Email addresses for correspondence: yuanxianxu@cardc.cn, xucx@tsinghua.edu.cn

1. Introduction

Shock wave/turbulent boundary layer interaction (SBLI) has been investigated extensively since the last century due to its significant importance in aerospace industries (Délery, Marvin & Reshotko 1986; Dolling 2001; Babinsky & Harvey 2011; Ligrani *et al.* 2020; Liu *et al.* 2022). When a supersonic turbulent boundary layer flow encounters a shock wave, the strong adverse pressure gradient induces abundant flow features, such as low-frequency unsteadiness (Clemens & Narayanaswamy 2014), acoustic radiations (Bernardini, Pirozzoli & Grasso 2011), local flow separation (Babinsky & Harvey 2011) and vortex shedding (Andreopoulos, Agui & Briassulis 2000; Tong *et al.* 2017; Fang *et al.* 2020). Despite this active research field going on for decades, there remain many open questions. For the oblique SBLI, supersonic flows over a compression corner and the impinging oblique shock wave on the turbulent boundary layers are two widely studied flow configurations. It has been proved that they share similar above-mentioned features within the interaction zone (Babinsky & Harvey 2011), with the latter free from the effects of the concave wall.

1.1. *Turbulence amplification and coherent structures*

One of the interesting phenomena in SBLI flows is 'turbulence amplification'. Early experimental studies (e.g. Smits & Muck 1987; Zheltovodov, Lebiga & Yakovlev 1989) showed that in supersonic flows over compression corners, where an oblique shock emerges due to the mean flow compression, the Reynolds stress is amplified. As the turning angle of the corner increases, the stronger compression leads to the increment of the pressure gradient, further resulting in higher amplification rates. Rose & Childs (1974) pointed out that the turbulence amplification is similar to the incompressible turbulent boundary layer flows under adverse pressure gradients. However, due to the compressibility effects, the turbulence amplification was believed to be caused by more than the adverse pressure gradient. Smits & Muck (1987) postulated that multiple plausible flow features might be responsible, such as the low-frequency shock motions, the direct shock wave/turbulence interaction (Zheltovodov *et al.* 1989), the generation of acoustic and entropy waves (Anyiwo & Bushnell 1982), the shear layer induced by the flow separation (Rose & Childs 1974; Selig *et al.* 1989), and the curvation of the streamlines (Andreopoulos *et al.* 2000). The direct numerical simulations (DNS) by Wu & Martin (2007, 2008) confirmed that the turbulence amplification can be attributed to the nonlinear coupling of vorticity, entropy, and the 'pumping' of turbulent fluctuations from the mean flow.

Owing to the advancement of experimental technologies and the enrichment of computational resources, some of the less important factors have been excluded (Fang *et al.* 2020). The shear layer related to the SBLI (referred to as the 'mixing layer' by some studies), is attributed primarily to the turbulence amplification. Dupont and coworkers have conducted a series of experiments on supersonic turbulent boundary layers impinged by an oblique shock wave (OSBLI) (Dupont *et al.* 2005, 2008; Dupont, Haddad & Debieve 2006). It was identified that the large-scale structures are formed near the end of the interaction zone where the shear layer reattaches, and are convected further downstream. The shear layer within the interaction zone shares commonalities with the compressible free shear layer, such as the spatial growth rate, entrainment velocity and turbulent shear stress, and their variation with the Mach number (Dupont, Piponniau & Dussauge 2019). Pirozzoli & Grasso (2006) and Pirozzoli & Bernardini (2011*a*) investigated the

OSBLI flows by DNS at the free-stream Mach number 2.3 and shock angle 33.2°, where the flow separation within the interaction zone is mild. The turbulence amplification is reckoned to be related to the shear layer, which thickens downstream due to the turbulent diffusion. The peaks of the Reynolds normal and shear stresses are located away from the wall in the outer region. The turbulence in the inner region returns to the equilibrium state quickly downstream, while the recovery to the equilibrium state in the outer region is not achieved even at the end of the computational domain. The vortex shedding adjacent to the separation zone induces the large-scale low-frequency unsteadiness downstream of the interaction zone. Dupont *et al.* (2008) and Helm, Martin & Dupont (2014) further confirmed this conclusion and stated that the existence of reverse flow and inflexional velocity profiles causes the Kelvin–Helmholtz instability, further leading to the development of large convective eddies. Pirozzoli, Bernardini & Grasso (2010) studied the transonic SBLI flows, where the shock wave is close to normal. Similar to OSBLI flows, when passing the impinging shock, the turbulence is amplified, the shear layer is developed and the shedding vortical structures are observed. In contrast to the OSBLI flows, they found that the streamwise velocity fluctuations are less affected compared with the cross-stream velocity fluctuations.

The exact mechanisms of the turbulence amplification are hard to trace from the chaotic turbulent fields. In this regard, the analysis of the turbulent kinetic energy (TKE) transport equation has shed some interesting light on this complicated phenomenon. Li *et al.* (2010) showed that in the supersonic turbulent flow over a compression ramp, the TKE production term increases rapidly within the separation zone, while the dissipation is significant only close to the wall. The energy transport is balanced by the mean flow convection and turbulent diffusion. Pirozzoli & Bernardini (2011*a*) provided similar descriptions for OSBLI flows. The maximum of the production term aligns with the mid-line of the shear layer within the interaction zone, due to the lift-up of vortical structures. Jammalamadaka, Li & Jaberi (2014) analysed the TKE and enstrophy transport equations along the sonic line. They proposed that the TKE amplification is caused by the increment of the TKE production and that the enstrophy amplification by the vortex stretching. The terms related to the compressibility effects, on the other hand, are negligible. Tong *et al.* (2017) conducted DNS for compression ramp flows at different turning angles, and found that the TKE transport in SBLI flows differs slightly from canonical wall-bounded turbulence in the small turning angle cases, while it is altered significantly by the shear layer above the separation bubble in the large turning angle cases. They also observed the destruction of low-speed streaks in the near-wall region and the emergence of the large-scale eddies adjacent to the shear layer. Humble, Scarano & Van Oudheusden (2007) and Fang *et al.* (2020) decomposed the TKE production term into the effects of mean flow deceleration and shear, based on which a novel mechanism for turbulence amplification was proposed. They attributed the turbulence amplification to the mean flow deceleration in the early stage, and the shear layer when it is well-developed. For the currently considered SBLI flows, the flows within the interaction zone are generally in non-equilibrium states (Pirozzoli *et al.* 2010; Zuo *et al.* 2019), hence the TKE budget would be effective in revealing the mechanism of turbulent amplification.

In another aspect, the physical counterparts of turbulence amplification are usually visible in the instantaneous fields. For flows over compression ramps, the Görtler vortices, the congenital secondary flows in turbulence over concave walls due to centrifugal instability (Saric 1994), are partially responsible for the amplification of turbulence (Loginov, Adams & Zheltovdov 2006). Priebe, Wu & Martin (2009) reported that the amplification rates in OSBLI flows are lower than those in the compression corner flows, which was attributed to the lack of the obvious streamline deflection. However, in

some recent numerical (Pasquariello, Hickel & Adams 2017) and experimental (Humble, Scarano & Van Oudheusden 2009; Zhuang *et al.* 2018) studies, it was argued that the large-scale quasi-streamwise vortices bear certain similarities to the Görtler vortices, which are referred to as the 'Görtler-like vortices'. Pasquariello *et al.* (2017) suggested the centrifugal instability induced by the streamline curvation to be a plausible mechanism for their generation. Zhuang *et al.* (2018) confirmed this idea by experiments. They further ascribed the neglect of the Görtler-like vortices in previous experiments to the long time period of oil-flow experiments such that those Görtler-like vortices are averaged out in the spanwise direction. Fang *et al.* (2020) observed that the near-wall low-speed streaks of the incoming turbulence are twisted within the interaction zone and regenerated downstream, less organized. Large-scale velocity streaks start to evidence near the shear layer in the outer region, and gradually decay downstream. Similar phenomena were also observed in transonic SBLI flows (Pirozzoli *et al.* 2010), where the near-wall low-speed streaks are suppressed near the interaction zone and regenerated downstream at approximately five interaction length scales. Among the few research works that provided the spanwise spectra, a recent experimental study by Baidya *et al.* (2020) found that the two energetic motions are prominent at large spanwise scales, which persist for a long streamwise extent.

As summarized previously, it is recognized that the turbulence amplification is caused by the mean flow deceleration and the shear layer, that the peaks of velocity fluctuation intensity are located with the shear layer downstream, and that the emergence of the large-scale structures is more or less related to the turbulence amplification. However, the association between turbulence amplification and the emergence of large-scale motions remains unclear. To unveil the direct link between these two phenomena, we propose to analyse the scale-by-scale TKE transport utilizing the TKE spectra transport equation. This will enable us to separate some of the flow features at certain length scales and investigate them individually, which will probably benefit our comprehension of this matter.

1.2. *Spectral analysis of TKE transport in wall-bounded turbulence*

The TKE spectra transport equation can be obtained by performing Fourier transforms on the transport equation of two-point correlation in the statistically homogeneous directions. Both of these equations have been applied to investigate the energy cascade in incompressible wall-bounded turbulence since the last century (Lumley 1964; Domaradzki *et al.* 1994). In recent years, this topic has been brought up again to reveal the inter-scale energy transfer in high-Reynolds-number channel flows. Lee & Moser (2015) analysed the TKE transport with the streamwise and spanwise spectra. The turbulent transport term is decomposed into turbulent diffusion in the wall-normal direction, and inter-scale energy transfer, whose integration is zero in spectral space. Inverse energy transfer from small- to large-scale motions in the buffer layer is observed in the spanwise TKE spectra. By integrating the turbulent diffusion term, Mizuno (2016) found that the upward turbulent transport provides energy to small-scale motions, while the large-scale downward energy fluxes bring energy to the near-wall region. Considering the statistical homogeneity in the streamwise and spanwise directions, Lee & Moser (2019) further analysed the spectra of TKE transport under the polar coordinate for the turbulent channel flow at $Re_\tau = 5200$. They found that the energy is transferred from the dominant streamwise very-large-scale motions to other velocity components via nonlinear interactions, and dissipated isotropically at small scales. Cho, Hwang & Choi (2018) performed triadic

wave interaction analysis to investigate the nonlinear interaction. Two new types of highly active inter-scale energy transfer processes in the near-wall region are found: from large to small scale by the interaction of large-scale and the adjacent small-scale motions, and from small to large scale by the downward energy transfer. Hamba (2019) further related the inverse energy cascade to the tilting of the streamwise vortices via conditional average.

On a more related subject, Auléry *et al.* (2015, 2017) derived the TKE spectra transport equation for flows with mean temperature variation, which can be regarded as the weakly compressible turbulence with negligible viscous dissipation. To incorporate the mean property variations caused by the mean temperature gradient in the definition of TKE spectra, the governing equation of the density-weighted velocity $v_i = \sqrt{\rho}\, u_i$ was derived, based on which the TKE spectra transport equation of v_i was obtained. The turbulent, pressure and viscous transport terms were split into the in-plane and inter-plane terms, consisting of only the derivatives in the wall-parallel and wall-normal directions, respectively. For the channel flow between a hot wall and a cold wall, in which the mean temperature gradient is significant, the total energy is transferred from the hot side to the cold side in the wall-normal direction, and the wall-parallel inter-scale energy transfer qualitatively resembles that in the canonical channel flows (Auléry *et al.* 2017). Dupuy, Toutant & Bataille (2018*a*,*b*) derived the TKE spectra transport equation relying on the insignificance of the density fluctuations in Morkovin's hypothesis. Therefore, the obtained equation is similar to that of the incompressible flows. However, in the presently considered flow, the density fluctuation may contribute largely to the kinetic energy near the shock wave. It is therefore inappropriate to adopt this method as well. Arun *et al.* (2021) derived the scale-space energy density transport equation for compressible inhomogeneous turbulent flows. They showed their work in detail on how to define the two-point correlation and energy density, and how to derive their transport equations. They further analysed the energy transfer in scale space for compressible mixing layer flows, and identified the scaling of the energy density function related to the self-similar evolution.

1.3. *Outline of the present study*

The primary goal of this paper is to explore the association between the turbulence amplification and the genesis of large-scale structures within the interaction zone in OSBLI flows. Considering the spanwise periodicity and homogeneity, we derive the TKE spectra transport equation from the spanwise two-point correlation transport equation. The scrutinization of the budget of the TKE spectra transport provides a scale-by-scale depiction of the energy production and transfer, which will benefit our understanding of the related physical processes.

The remainder of this paper is arranged as follows. The physical model, numerical implements and validations are introduced in § 2. The transport equations of two-point correlation and TKE spectra are derived in § 3 as the mathematical tools for analyses. The coherent structures in the instantaneous fields and the TKE amplification are discussed briefly in § 4 to compare with the conclusions in previous studies. The TKE spectra distribution is presented in § 5 to relate the emergence of large-scale motions and turbulence amplification. The energy transfer process for finite spanwise scale motions and the spanwise uniform motions are revealed in §§ 6 and 7, respectively. Concluding remarks are given in § 8.

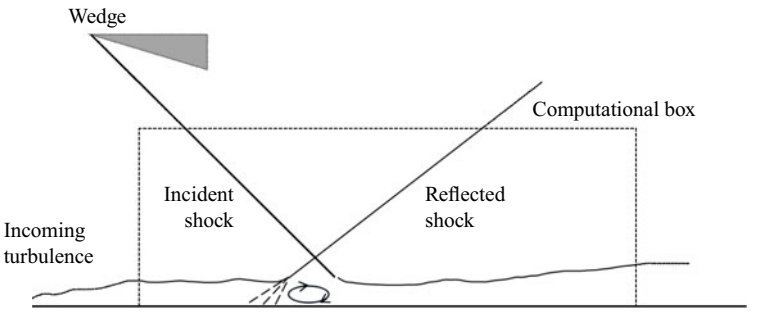

Figure 1. Sketch of physical model and computational domain.

2. Numerical settings and validation

2.1. *Physical model and numerical settings*

The sketch of the physical model and computational domain is depicted in figure 1. We simulate the fully-developed supersonic turbulent boundary layer impinged by an oblique shock wave. The mean velocity profile of the incoming turbulence is described according to Musker (1979), and the velocity fluctuations are generated by the synthetic digital filtering approach (Klein, Sadiki & Janicka 2003). The mean temperature and temperature fluctuations are given according to the generalized Reynolds analogy (Zhang *et al.* 2014). The oblique shock is generated at the top boundary by imposing the inviscid Rankine–Hugoniot jump condition to simulate the effect of a wedge shock generator with deflection angle 8°. The generated shock angle is 33.2°, and the impingement point is $x_{imp} = 30\delta_{in}$ (where δ_{in} is the nominal boundary layer thickness at the inlet). The upper and outflow boundaries are enforced by non-reflecting conditions (Pirozzoli & Colonius 2013). At the lower wall, no-slip and no-penetration conditions are applied for velocity, and the isothermal condition is applied for temperature, with the wall temperature set as the recovery temperature $T_w = 1.92T_\infty$ to achieve a quasi-adiabatic thermal boundary condition. Periodic conditions are applied in the spanwise direction.

We solve directly the three-dimensional Navier–Stokes equations for compressible Newtonian gas with the finite difference method. The DNS are performed with the open-source 'STREAmS' solver developed by Bernardini *et al.* (2021), which has been validated widely for solving compressible channel, boundary layer, and especially OSBLI flows (e.g. Bernardini *et al.* 2016; Volpiani, Bernardini & Larsson 2020). The convective terms are approximated by the sixth-order kinetic-energy-preserving scheme (Pirozzoli 2010), and switched to the fifth-order WENO scheme (Jiang & Shu 1996) near strong flow compression, which is identified by the criterion of Ducros *et al.* (1999). The viscous terms are cast as Laplacian forms and approximated by the sixth-order central difference scheme. Time advancement is achieved by Wray's three-stage third-order scheme (Wray 1990).

The free-stream Mach number of the inflow is set as $M_\infty = 2.28$, and the Reynolds number is set as $Re_{in} = \rho_\infty U_\infty \delta_{in}/\mu_\infty = 12\,000$, with ρ_∞, U_∞ and μ_∞ denoting the free-stream density, velocity and dynamic viscosity coefficients, and δ_{in} the nominal thickness of the incoming boundary layer. The sizes of the computational domain in the streamwise (x), wall-normal (y) and spanwise (z) directions are $(L_x, L_y, L_z) = (60\delta_{in}, 12\delta_{in}, 6.5\delta_{in})$, respectively. The computational domain is discretized by (2000, 320, 240) grids in the three directions. The grids are uniformly distributed in the x and z directions, with the mesh intervals under the viscous scales (defined below)

M_∞	C_{f0}	δ_0^*/δ_0	θ_0/δ_0	$Re_{\theta 0}$	$Re_{\delta 2,0}$	$Re_{\tau 0}$	H_0	H_{i0}
2.28	3.104×10^{-3}	0.334	0.0902	982	567	201	3.70	1.54

Table 1. Statistical properties at the reference plane $x = 15.0\delta_{in}$. Here, $C_f = 2\tau_w/(\rho_\infty U_\infty^2)$, $Re_{\theta 0} = \rho_\infty U_\infty \theta_0/\mu_\infty$, $Re_{\delta 2,0} = \rho_\infty U_\infty \theta_0/\mu_w$, $H_0 = \delta_0^*/\theta_0$ and $H_{i0} = \delta_{i0}^*/\theta_{i0}$.

being $\Delta x^+ \approx 5.4$ and $\Delta z^+ \approx 4.9$. In the wall-normal direction, the grids are stretched by a hyperbolic-sine function within $y = 2.5\delta_{in}$, with the first off-wall grid located at $\Delta y_w^+ \approx 0.7$, and uniformly distributed above it, with grid interval $\Delta y^+ \approx 7.0$. According to the DNS performed by Volpiani, Bernardini & Larsson (2018) under roughly the same flow parameters and numerical conditions, the grid intervals in the present study are fine enough to obtain accurate results.

The statistics are averaged in the spanwise direction with 900 instantaneous flow fields over the period $600\delta_{in}/U_\infty$. To further obtain smoother statistics, the average in the streamwise direction is also adopted across 11 grids, within which the streamwise variation of the mean flow is insignificant, even inside the interaction zone. The ensemble average of a generic variable φ is denoted as $\bar{\varphi}$, and the corresponding fluctuation by φ', the density-weighted average (or Favre average) by $\tilde{\varphi}$, and the corresponding fluctuation φ''.

2.2. *Basic flow statistics and validation*

We take the streamwise location at $x = 15.0\delta_{in}$ as the reference plane (denoted by x_0), where the turbulence is free from the impact of the impinging shock wave. The statistical properties at x_0 (hereinafter denoted by the subscript 0) are listed in table 1. The friction Reynolds number Re_τ is defined as

$$Re_\tau = \frac{\rho_w u_\tau \delta_0}{\mu_w}, \tag{2.1}$$

with

$$u_\tau = \sqrt{\frac{\tau_w}{\rho_w}}, \quad \tau_w = \mu_w \left.\frac{\partial \bar{u}}{\partial y}\right|_w, \tag{2.2a,b}$$

where ρ_w and μ_w denote the mean density and dynamic viscosity on the wall, and τ_w denotes the mean wall shear stress. The displacement and momentum thicknesses, denoted as δ^* and θ, are defined as

$$\delta^* = \int_0^\delta \left(1 - \frac{\bar{\rho}\bar{u}}{\rho_\infty U_\infty}\right) \mathrm{d}y, \quad \theta = \int_0^\delta \frac{\bar{\rho}\bar{u}}{\rho_\infty U_\infty}\left(1 - \frac{\bar{u}}{U_\infty}\right) \mathrm{d}y. \tag{2.3a,b}$$

The incompressible boundary layer thicknesses, denoted by δ_i^* and θ_i, along with the incompressible shape factor H_i, are defined accordingly by setting the mean density ratio as unity.

The van-Driest-transformed mean velocity and Reynolds stress under viscous scales in (2.2*a*,*b*) are defined as

$$u_{VD}^+ = \int_0^{\bar{u}^+} \sqrt{\frac{\bar{\rho}}{\rho_w}}\, \mathrm{d}\bar{u}^+, \quad R_{ij}^* = \frac{\overline{\rho u_i'' u_j''}}{\tau_w}, \tag{2.4a,b}$$

where the superscript $+$ represents the normalization by u_τ as incompressible flows. The distributions at x_0 are displayed in figure 2 against the wall-normal coordinate under

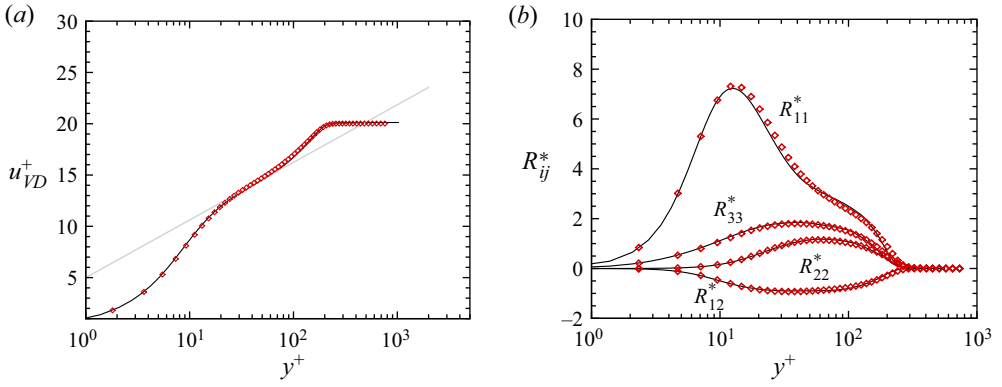

Figure 2. Wall-normal distributions of (*a*) van-Driest-transformed mean velocity and (*b*) Reynolds stress. Lines indicate results at $x_0 = 15\delta_{in}$; symbols indicate reference data in Pirozzoli & Bernardini (2011*b*) at $M_0 = 2.0$, $Re_\tau \approx 200$.

viscous scale $y^+ = y\,Re_\tau/\delta_0$, and compared with those of supersonic turbulent boundary layers at $M_\infty = 2.0$ and $Re_\tau \approx 200$ reported by Pirozzoli & Bernardini (2011*b*). The wall-normal distributions of both the mean velocity and Reynolds stress in the present study agree reasonably well with the reference, indicating the validity of the current results. It also suggests that the turbulence at the reference station x_0 is fully developed.

We further report the skin friction coefficient C_f and mean wall pressure $\bar{p}_w$ distribution along the streamwise (x) direction, with the former defined as

$$C_f = \frac{2\tau_w}{\rho_\infty U_\infty^2}. \tag{2.5}$$

The subsequent results will be reported under the scaled interaction coordinate, i.e. $x^* = (x - x_{imp})/\delta_0$ and $y^* = y/\delta_0$, as usually adopted in SBLI flow analysis. The streamwise distribution of C_f is presented in figure 3(*a*). It can be identified that the streamwise locations of the flow separation and reattachment points are $x^*_s \approx -2.60$ and $x^*_r \approx -0.73$, where $C_f = 0$. The extrapolated origin of the reflected shock in the mean velocity field is located at $x^*_i \approx -3.27$. Therefore, the lengths of the interaction and separation zones are $L^*_{int} = x^*_i \approx 3.27$ and $L^*_{sep} = x^*_r - x^*_s \approx 1.87$, respectively. These values are consistent with the results reported in Volpiani *et al.* (2018, figure 12). The mean wall pressure $\bar{p}_w$ distribution is presented in figure 3(*b*), along with the DNS results reported by Pirozzoli & Bernardini (2011*a*) and the inviscid theory. The presently obtained result generally collapses with the reference data. The wall pressure increases rapidly at the start of the interaction zone and gradually reaches the theoretical inviscid solution. The preceding results confirmed the accuracy of the present DNS statistics.

3. Derivation of TKE spectra transport equation

In this section, we first derive the transport equation of spanwise two-point correlation. The equation for TKE spectra transport is further obtained via Fourier transform.

3.1. *Two-point correlation transport equation*

We first derive the transport equation of spanwise two-point correlation, considering the statistical homogeneity and periodicity in that direction. According to Arun *et al.* (2021),

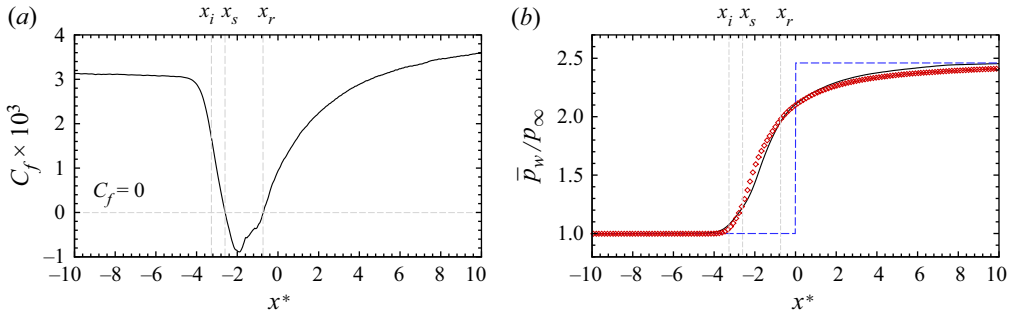

Figure 3. Wall statistics: (*a*) skin friction C_f, (*b*) mean pressure $\bar{p}_w$. Red symbols indicate reference data from Pirozzoli & Bernardini (2011*a*); blue dashed lines indicate the inviscid solution; x_i, x_s and x_r are the locations of the extrapolated origin of the reflected shock, the separation and the reattachment point, respectively.

the fluctuation of momentum equation can be cast as

$$\frac{\partial \rho u_i''}{\partial t} + \frac{\partial \rho u_i''(\tilde{u}_k + u_k'')}{\partial x_k} + \rho u_k'' \frac{\partial \tilde{u}_i}{\partial x_k} = -\frac{\partial p'}{\partial x_i} + \frac{\partial \tau_{ik}'}{\partial x_k} + \left(1 - \frac{\rho}{\bar{\rho}}\right)\left(-\frac{\partial \bar{p}}{\partial x_i} + \frac{\partial \bar{\tau}_{ik}}{\partial x_k}\right) + \frac{\rho}{\bar{\rho}} \frac{\partial \bar{\rho} R_{ik}}{\partial x_k}. \tag{3.1}$$

Note that this equation is obtained by combining the fluctuation of momentum equation in non-conservative form and the continuity equation. The spanwise two-point correlation tensor between velocity components u_i'' at $\boldsymbol{x} = (x, y, z)$ and u_j'' at $(\boldsymbol{x} + \boldsymbol{r}) = (x, y, z + r_z)$ is defined as (Arun *et al.* 2021)

$$Q_{ij}(\boldsymbol{x}, \boldsymbol{r}) = \frac{1}{2} \overline{(\rho(\boldsymbol{x}) + \rho(\boldsymbol{x} + \boldsymbol{r}))\, u_i''(\boldsymbol{x})\, u_j''(\boldsymbol{x} + \boldsymbol{r})}, \tag{3.2}$$

which is a function of x, y and r_z. The derivation of the Q_{ij} transport equation is similar to that in the incompressible flows. The derivatives in the z direction at $\boldsymbol{x}$ and $\tilde{\boldsymbol{x}} = \boldsymbol{x} + \boldsymbol{r}$ are related by r_z (Lee & Moser 2019):

$$\frac{\partial}{\partial z} = -\frac{\partial}{\partial r_z}, \quad \frac{\partial}{\partial \tilde{z}} = \frac{\partial}{\partial r_z}. \tag{3.3a,b}$$

Moreover, the averaged flow quantities are independent of r_z, i.e.

$$\bar{\varphi}(\boldsymbol{x}) = \bar{\varphi}(\boldsymbol{x} + \boldsymbol{r}), \quad \tilde{\varphi}(\boldsymbol{x}) = \tilde{\varphi}(\boldsymbol{x} + \boldsymbol{r}). \tag{3.4a,b}$$

After a detailed derivation, we formulate the transport equation for two-point correlation tensor as

$$\frac{\partial Q_{ij}(\boldsymbol{x}, \boldsymbol{r})}{\partial t} = C_{ij} + P_{ij} + D_{ij} + \Pi_{ij} + \varepsilon_{ij} + T_{ij} + B_{ij}. \tag{3.5}$$

The terms on the right-hand side represent the contributions from the mean flow convection, production, diffusion, pressure-strain, viscous dissipation, inter-scale transfer and mass-diffusion, respectively. The convection and production terms are related to the

variation of mean velocity:

$$C_{ij} = -\frac{\partial}{\partial x_k} Q_{ij}(\boldsymbol{x}, \boldsymbol{r})\, \tilde{u}_k(\boldsymbol{x}) \quad (k = 1, 2), \tag{3.6}$$

$$P_{ij} = -Q_{kj}(\boldsymbol{x}, \boldsymbol{r})\, \frac{\partial \tilde{u}_i(\boldsymbol{x})}{\partial x_k} - Q_{ik}(\boldsymbol{x}, \boldsymbol{r}) \frac{\partial \tilde{u}_j(\boldsymbol{x})}{\partial x_k} \quad (k = 1, 2). \tag{3.7}$$

The diffusion term D_{ij} involves the diffusion by turbulent transport D_{ij}^T, pressure fluctuation D_{ij}^P, and viscous stress fluctuation D_{ij}^V:

$$D_{ij}^T = -\frac{1}{4} \frac{\partial}{\partial x_k} \overline{(\rho(\boldsymbol{x}) + \rho(\boldsymbol{x}+\boldsymbol{r}))\, u_i''(\boldsymbol{x})\, u_j''(\boldsymbol{x}+\boldsymbol{r})\, (u_k''(\boldsymbol{x}) + u_k''(\boldsymbol{x}+\boldsymbol{r}))} \quad (k = 1, 2), \tag{3.8}$$

$$D_{ij}^P = -\frac{1}{2} \left(\overline{\left(1 + \frac{\rho(\boldsymbol{x}+\boldsymbol{r})}{\rho(\boldsymbol{x})}\right) \frac{\partial p'(\boldsymbol{x})\, u_j''(\boldsymbol{x}+\boldsymbol{r})}{\partial x_k}}\, \delta_{ik} + \overline{\left(1 + \frac{\rho(\boldsymbol{x})}{\rho(\boldsymbol{x}+\boldsymbol{r})}\right) \frac{\partial p'(\boldsymbol{x}+\boldsymbol{r})\, u_i''(\boldsymbol{x})}{\partial x_k}}\, \delta_{jk} \right), \tag{3.9}$$

$$D_{ij}^V = \frac{1}{2} \left(\overline{\left(1 + \frac{\rho(\boldsymbol{x}+\boldsymbol{r})}{\rho(\boldsymbol{x})}\right) \frac{\partial \tau_{ik}'(\boldsymbol{x})\, u_j''(\boldsymbol{x}+\boldsymbol{r})}{\partial x_k}} + \overline{\left(1 + \frac{\rho(\boldsymbol{x})}{\rho(\boldsymbol{x}+\boldsymbol{r})}\right) \frac{\partial \tau_{jk}'(\boldsymbol{x}+\boldsymbol{r})\, u_i''(\boldsymbol{x})}{\partial x_k}} \right) \quad (k = 1, 2). \tag{3.10}$$

The pressure-strain term Π_{ij} reflects the inter-component energy transfer:

$$\Pi_{ij} = \frac{1}{2} \left(\overline{\left(1 + \frac{\rho(\boldsymbol{x}+\boldsymbol{r})}{\rho(\boldsymbol{x})}\right) p'(\boldsymbol{x}) \frac{\partial u_j''(\boldsymbol{x}+\boldsymbol{r})}{\partial x_i}} + \overline{\left(1 + \frac{\rho(\boldsymbol{x})}{\rho(\boldsymbol{x}+\boldsymbol{r})}\right) p'(\boldsymbol{x}+\boldsymbol{r}) \frac{\partial u_i''(\boldsymbol{x})}{\partial x_j}} \right). \tag{3.11}$$

The dissipation by viscosity ε_{ij} is expressed as

$$\varepsilon_{ij} = -\frac{1}{2} \left(\overline{\left(1 + \frac{\rho(\boldsymbol{x}+\boldsymbol{r})}{\rho(\boldsymbol{x})}\right) \tau_{ik}'(\boldsymbol{x}) \frac{\partial u_j''(\boldsymbol{x}+\boldsymbol{r})}{\partial x_k}} + \overline{\left(1 + \frac{\rho(\boldsymbol{x})}{\rho(\boldsymbol{x}+\boldsymbol{r})}\right) \tau_{jk}'(\boldsymbol{x}+\boldsymbol{r}) \frac{\partial u_i''(\boldsymbol{x})}{\partial x_k}} \right) \quad (k = 1, 2, 3). \tag{3.12}$$

The inter-scale energy transfer, corresponding to the nonlinear turbulent interactions in incompressible flows (Domaradzki *et al.* 1994; Mizuno 2016; Lee & Moser 2019), can be

split as $T_{ij} = T_{ij}^{xy} + T_{ij}^{z}$, where

$$T_{ij}^{xy} = -\frac{1}{2}\overline{u_j''(\boldsymbol{x}+\boldsymbol{r})\,\frac{\partial \rho(\boldsymbol{x})\,u_i''(\boldsymbol{x})\,u_k''(\boldsymbol{x})}{\partial x_k}} - \frac{1}{2}\overline{\rho(\boldsymbol{x}+\boldsymbol{r})\,u_j''(\boldsymbol{x}+\boldsymbol{r})\,u_k''(\boldsymbol{x})\,\frac{\partial u_i''(\boldsymbol{x})}{\partial x_k}}$$
$$- \frac{1}{2}\overline{u_i''(\boldsymbol{x})\,\frac{\partial \rho(\boldsymbol{x}+\boldsymbol{r})\,u_j''(\boldsymbol{x}+\boldsymbol{r})\,u_k''(\boldsymbol{x}+\boldsymbol{r})}{\partial x_k}} - \frac{1}{2}\overline{\rho(\boldsymbol{x})\,u_i''(\boldsymbol{x})\,u_k''(\boldsymbol{x}+\boldsymbol{r})\,\frac{\partial u_j''(\boldsymbol{x}+\boldsymbol{r})}{\partial x_k}}$$
$$- D_{ij}^{T} \quad (k=1,2), \tag{3.13}$$

$$T_{ij}^{z} = -\frac{1}{2}\frac{\partial}{\partial r_z}\overline{(\rho(\boldsymbol{x})+\rho(\boldsymbol{x}+\boldsymbol{r}))\,u_i''(\boldsymbol{x})\,u_j''(\boldsymbol{x}+\boldsymbol{r})\,(w''(\boldsymbol{x}+\boldsymbol{r})-w''(\boldsymbol{x}))}$$
$$- \frac{1}{2}\overline{u_i''(\boldsymbol{x})\,u_j''(\boldsymbol{x}+\boldsymbol{r})\,\frac{\partial}{\partial r_z}(\rho(\boldsymbol{x})\,w''(\boldsymbol{x}+\boldsymbol{r})-\rho(\boldsymbol{x}+\boldsymbol{r})\,w''(\boldsymbol{x}))}. \tag{3.14}$$

Complicated as it is, we can easily prove that $T_{ij} \to 0$ at the limit of $r_z \to 0$, indicating that this term is responsible only for the inter-scale energy transfer. Finally, the mass-diffusion B_{ij}, caused by the density fluctuation, can be cast as

$$B_{ij} = \frac{1}{2}\left(\overline{u_j''(\boldsymbol{x}+\boldsymbol{r})} - \frac{\overline{\rho(\boldsymbol{x})\,u_j''(\boldsymbol{x}+\boldsymbol{r})}}{\bar{\rho}(\boldsymbol{x})} + \frac{\overline{\rho(\boldsymbol{x}+\boldsymbol{r})\,u_j''(\boldsymbol{x}+\boldsymbol{r})}}{\rho(\boldsymbol{x})}\right)\left(-\frac{\partial \bar{p}}{\partial x_i} + \frac{\partial \bar{\tau}_{ik}}{\partial x_k}\right)$$
$$+ \frac{1}{2}\left(\overline{u_i''(\boldsymbol{x})} - \frac{\overline{\rho(\boldsymbol{x}+\boldsymbol{r})\,u_i''(\boldsymbol{x})}}{\bar{\rho}(\boldsymbol{x})} + \frac{\overline{\rho(\boldsymbol{x})\,u_i''(\boldsymbol{x})}}{\rho(\boldsymbol{x}+\boldsymbol{r})}\right)\left(-\frac{\partial \bar{p}}{\partial x_j} + \frac{\partial \bar{\tau}_{jk}}{\partial x_k}\right)$$
$$- \frac{1}{2}\left(\frac{\overline{\rho(\boldsymbol{x})\,u_j''(\boldsymbol{x}+\boldsymbol{r})}}{\bar{\rho}(\boldsymbol{x})} + \frac{\overline{\rho(\boldsymbol{x}+\boldsymbol{r})u_j''(\boldsymbol{x}+\boldsymbol{r})}}{\rho(\boldsymbol{x})}\right)\frac{\partial \bar{\rho} R_{ik}}{\partial x_k}$$
$$- \frac{1}{2}\left(\frac{\overline{\rho(\boldsymbol{x}+\boldsymbol{r})\,u_i''(\boldsymbol{x})}}{\bar{\rho}(\boldsymbol{x})} + \frac{\overline{\rho(\boldsymbol{x})\,u_i''(\boldsymbol{x})}}{\rho(\boldsymbol{x}+\boldsymbol{r})}\right)\frac{\partial \bar{\rho} R_{jk}}{\partial x_k}. \tag{3.15}$$

The equations above degenerate to the TKE transport equation by taking $r_z = 0$ and contracting the indices i and j, and to the two-point correlation transport equation for incompressible flows by taking the density as unity.

3.2. *Spectra of Reynolds stress transport*

As customarily performed in the incompressible turbulence (e.g. Lee & Moser 2015), the transport equation of the Reynolds stress spectra can be obtained by performing a Fourier transform on the two-point correlation transport equation. According to the definition in (3.2), the spectra of the Reynolds stress tensor can be expressed as

$$\hat{Q}_{ij} = \mathrm{Re}\left[\widehat{\rho u_i''}\,\widehat{u_j''}^{\star} + \widehat{u_i''}\,\widehat{\rho u_j''}^{\star}\right], \tag{3.16}$$

where the hat symbol denotes Fourier spectral coefficients, the superscript $\star$ indicates the complex conjugate, and Re represents taking the averaged real part. The budget terms of

(3.5) are transformed into spectral space accordingly. The convection and production terms in (3.6) and (3.7) are therefore transformed as

$$\hat{C}_{ij} = -\frac{\partial}{\partial x_k}\hat{Q}_{ij}\tilde{u}_k, \tag{3.17}$$

$$\hat{P}_{ij} = -\hat{Q}_{kj}\frac{\partial \tilde{u}_i}{\partial x_k} - \hat{Q}_{ik}\frac{\partial \tilde{u}_j}{\partial x_k}. \tag{3.18}$$

The other budget terms are nonlinear, primarily due to the density variation. Taking the turbulent diffusion term D_{ij}^T in (3.8) as an example, we reformulate all of those terms according to the independent variable

$$\begin{aligned} D_{ij}^T = -\frac{1}{4}\frac{\partial}{\partial x_k}(&\overline{\rho(\boldsymbol{x})\,u_i''(\boldsymbol{x})\,u_k''(\boldsymbol{x})\,u_j''(\boldsymbol{x}+\boldsymbol{r})} + \overline{u_i''(\boldsymbol{x})\,u_k''(\boldsymbol{x})\,\rho(\boldsymbol{x}+\boldsymbol{r})\,u_j''(\boldsymbol{x}+\boldsymbol{r})} \\ &+ \overline{\rho(\boldsymbol{x})\,u_i''(\boldsymbol{x})\,u_j''(\boldsymbol{x}+\boldsymbol{r})\,u_k''(\boldsymbol{x}+\boldsymbol{r})} + \overline{u_i''(\boldsymbol{x})\,\rho(\boldsymbol{x}+\boldsymbol{r})\,u_j''(\boldsymbol{x}+\boldsymbol{r})\,u_k''(\boldsymbol{x}+\boldsymbol{r})}), \end{aligned} \tag{3.19}$$

therefore its Fourier transform is expressed as

$$\hat{D}_{ij}^T = -\frac{1}{4}\frac{\partial}{\partial x_k}\mathrm{Re}\left[\widehat{\rho u_i'' u_k''}\,\widehat{u_j''}^{\star} + \widehat{u_i'' u_k''}\,\widehat{\rho u_j''}^{\star} + \widehat{\rho u_i''}\,\widehat{u_j'' u_k''}^{\star} + \widehat{u_i''}\,\widehat{\rho u_j'' u_k''}^{\star}\right]. \tag{3.20}$$

The pressure diffusion, viscous diffusion, pressure-strain and viscous dissipation terms in (3.9), (3.10), (3.11) and (3.12) are correspondingly transformed as

$$\begin{aligned} \hat{D}_{ij}^P = &-\frac{1}{2}\mathrm{Re}\left[\widehat{\frac{\partial p'}{\partial x_i}}\,\widehat{u_j''}^{\star} + \widehat{\frac{\partial p'}{\partial x_j}}^{\star}\,\widehat{u_i''} + \widehat{p'}\,\widehat{\frac{\partial u_j''}{\partial x_i}}^{\star} + \widehat{p'}^{\star}\,\widehat{\frac{\partial u_i''}{\partial x_j}}\right] \\ &-\frac{1}{2}\mathrm{Re}\left[\widehat{\frac{1}{\rho}\frac{\partial p'}{\partial x_i}}\,\widehat{\rho u_j''}^{\star} + \widehat{\frac{1}{\rho}\frac{\partial p'}{\partial x_j}}^{\star}\,\widehat{\rho u_i''} + \widehat{\frac{p'}{\rho}}\,\widehat{\rho\frac{\partial u_j''}{\partial x_i}}^{\star} + \widehat{\frac{p'}{\rho}}^{\star}\,\widehat{\rho\frac{\partial u_i''}{\partial x_j}}\right], \end{aligned} \tag{3.21}$$

$$\begin{aligned} \hat{D}_{ij}^V = &\frac{1}{2}\mathrm{Re}\left[\widehat{\frac{\partial \tau_{ik}'}{\partial x_k}}\,\widehat{u_j''}^{\star} + \widehat{\frac{\partial \tau_{jk}'}{\partial x_k}}^{\star}\,\widehat{u_i''} + \widehat{\tau_{ik}'}\,\widehat{\frac{\partial u_j''}{\partial x_k}}^{\star} + \widehat{\tau_{jk}'}^{\star}\,\widehat{\frac{\partial u_i''}{\partial x_k}}\right] \\ &+\frac{1}{2}\mathrm{Re}\left[\widehat{\frac{1}{\rho}\frac{\partial \tau_{ik}'}{\partial x_k}}\,\widehat{\rho u_j''}^{\star} + \widehat{\frac{1}{\rho}\frac{\partial \tau_{jk}'}{\partial x_k}}^{\star}\,\widehat{\rho u_i''} + \widehat{\frac{\tau_{ik}'}{\rho}}\,\widehat{\rho\frac{\partial u_j''}{\partial x_k}}^{\star} + \widehat{\frac{\tau_{jk}'}{\rho}}^{\star}\,\widehat{\rho\frac{\partial u_i''}{\partial x_k}}\right], \end{aligned} \tag{3.22}$$

$$\hat{\Pi}_{ij} = \frac{1}{2}\mathrm{Re}\left[\widehat{p'}\,\widehat{\frac{\partial u_j'}{\partial x_i}}^{\star} + \widehat{p'}^{\star}\,\widehat{\frac{\partial u_i'}{\partial x_j}} + \widehat{\frac{p'}{\rho}}\,\widehat{\rho\frac{\partial u_j'}{\partial x_i}}^{\star} + \widehat{\frac{p'}{\rho}}^{\star}\,\widehat{\rho\frac{\partial u_i'}{\partial x_j}}\right], \tag{3.23}$$

$$\hat{\varepsilon}_{ij} = -\frac{1}{2}\mathrm{Re}\left[\widehat{\tau_{ik}'}\,\widehat{\frac{\partial u_j'}{\partial x_k}}^{\star} + \widehat{\tau_{jk}'}^{\star}\,\widehat{\frac{\partial u_i'}{\partial x_k}} + \widehat{\frac{\tau_{ik}'}{\rho}}\,\widehat{\rho\frac{\partial u_j'}{\partial x_k}}^{\star} + \widehat{\frac{\tau_{jk}'}{\rho}}^{\star}\,\widehat{\rho\frac{\partial u_i'}{\partial x_k}}\right]. \tag{3.24}$$

For the inter-scale energy transfer term, the T_{ij}^{xy} component is transformed as

$$\hat{T}_{ij}^{xy} = -\frac{1}{2}\,\mathrm{Re}\left[\widehat{\frac{\partial \rho u_i'' u_k''}{\partial x_k}}\,\widehat{u_j''}^{\star} + \widehat{u_k''\frac{\partial u_i''}{\partial x_k}}\,\widehat{\rho u_j''}^{\star} + \widehat{\frac{\partial \rho u_j'' u_k''}{\partial x_k}}^{\star}\,\widehat{u_i''} + \widehat{u_k''\frac{\partial u_j''}{\partial x_k}}^{\star}\,\widehat{\rho u_i''}\right] - \hat{D}_{ij}^{T} \quad (k = 1, 2), \tag{3.25}$$

and T_{ij}^{z} as

$$\hat{T}_{ij}^{z} = \frac{1}{2}\,k_z\,\mathrm{Im}\left[\widehat{\rho u_i''\,u_j''w''}^{\star} - \widehat{\rho u_i''w''}\,\widehat{u_j''}^{\star} + \widehat{\rho u_j''w''}^{\star}\,\widehat{u_i''} - \widehat{\rho u_j''}^{\star}\,\widehat{u_i''w''}\right] - \frac{1}{2}\,\mathrm{Re}\left[\widehat{w''\frac{\partial u_i''}{\partial z}}\,\widehat{\rho u_j''}^{\star} + \widehat{\rho u_i''}\,\widehat{w''\frac{\partial u_j''}{\partial z}}^{\star}\right], \tag{3.26}$$

where Im denotes taking the averaged imaginary part, and k_z represents the spanwise wavenumber. Finally, the transformed mass-flux term is formulated as

$$\begin{aligned}\hat{B}_{ij} = {} & \frac{1}{2}\,\mathrm{Re}\left[\widehat{u_j''}^{\star} - \frac{\hat{\rho}\,\widehat{u_j''}^{\star}}{\bar{\rho}} + \frac{\widehat{1}}{\rho}\,\widehat{\rho u_j''}^{\star}\right]\left(-\frac{\partial \bar{p}}{\partial x_i} + \frac{\partial \bar{\tau}_{ik}}{\partial x_k}\right) \\ & + \frac{1}{2}\,\mathrm{Re}\left[\widehat{u_i''} - \frac{\hat{\rho}^{\star}\,\widehat{u_i''}}{\bar{\rho}} + \frac{\widehat{1}^{\star}}{\rho}\,\widehat{\rho u_i''}\right]\left(-\frac{\partial \bar{p}}{\partial x_j} + \frac{\partial \bar{\tau}_{jk}}{\partial x_k}\right) \\ & + \frac{1}{2}\,\mathrm{Re}\left[\frac{\hat{\rho}\,\widehat{u_j''}^{\star}}{\bar{\rho}} + \frac{\widehat{1}}{\rho}\,\widehat{\rho u_j''}^{\star}\right]\frac{\partial \bar{\rho} R_{ik}}{\partial x_k} + \frac{1}{2}\,\mathrm{Re}\left[\frac{\hat{\rho}^{\star}\,\widehat{u_i''}}{\bar{\rho}} + \frac{\widehat{1}^{\star}}{\rho}\,\widehat{\rho u_i''}\right]\frac{\partial \bar{\rho} R_{jk}}{\partial x_k}.\end{aligned} \tag{3.27}$$

Contracting indices i and j of the tensor $\hat{Q}_{ij}$, the transport equation of TKE spectra $\hat{Q}_{kk}$ is obtained, which will be considered primarily in the subsequent discussions.

4. Coherent structures and turbulence amplification

As a first impression of the association between the turbulence amplification and its physical counterparts, we present the instantaneous fields of low-speed streaks in figure 4(*a*) and vortical structures in figure 4(*b*), the latter represented by the second invariant Q of the velocity gradient. Upstream of the interaction zone, both the low-speed streaks and vortical structures resemble those in the low-Reynolds-number turbulent boundary layer flows. These structures go through rapid change across the interaction zone, where the small-scale low-speed streaks are twisted and weakened, while the large-scale structures emerge. Similar phenomena have been reported by previous studies, such as Zhuang *et al.* (2018) and Fang *et al.* (2020). Although mean flow separation and spanwise vortex shedding are barely noticeable, the abundant vortical structures are populated within the interaction zone. This will be analysed further in the following discussions. In the post-shock region, the turbulence relaxes gradually to the equilibrium state, where the near-wall small-scale structures are regenerated, and the large-scale structures in the outer

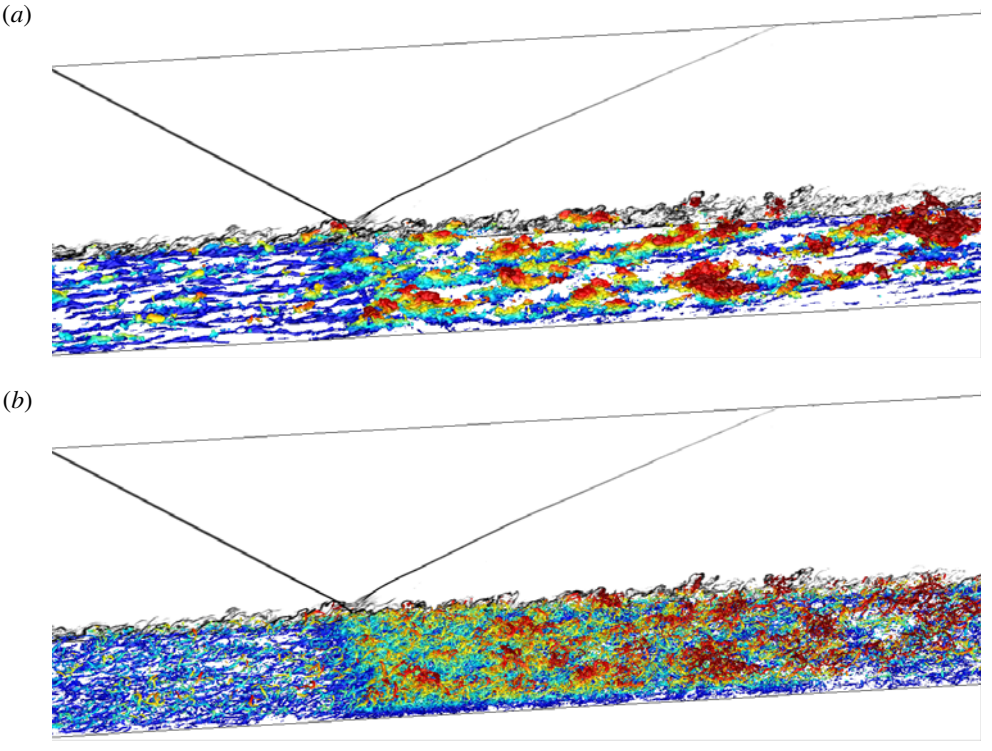

Figure 4. Instantaneous fields, isosurface of (*a*) velocity fluctuation $u'/U_\infty = -0.1$, (*b*) the second invariant of velocity gradient $Q = 10.0$, coloured by the wall-normal coordinate. Vertical slices are numerical schlieren, flooded by $NS = \exp(-|\nabla\rho|/\rho)$.

region are weakened. As demonstrated by Pirozzoli & Grasso (2006), the relaxation to the equilibrium state for large-scale motions in the outer region requires a long streamwise extent. This process will be considered in our subsequent research.

The components of the Reynolds stress tensor near the interaction zone, normalized by $\rho_\infty U_\infty^2$, are displayed in figure 5. The R_{uu} component (figure 5*a*), representing the density-weighted variance of u'', increases remarkably as it approaches the interaction zone. The peak location rises to detach from the wall along with the average sonic line. In the streamwise direction, it reaches maxima at $x^* \approx -1.5$, where it starts to decay. In the post-shock region, the wall-normal locations of the peaks lie at $y^* \approx 0.4$ and rise slightly along x^*. A secondary peak near the wall emerges downstream of the interaction zone at $x^* \approx 3.5$, indicating that the near-wall velocity streaks are regenerated. The R_{vv} and R_{ww} components, shown in figures 5(*b*,*c*), also increase within the interaction zone and attain maxima at $x^* \approx 0$ and $x^* \approx -1.5$, respectively. Their evolutions downstream resemble that of the R_{uu} component, except for the slower decay rates. Based on this scenario, the emergence of the strong streamwise vortices or cross-stream circulations composed of v'' and w'' is expected in the post-shock region. The amplification of the Reynolds shear stress R_{uv} (figure 5*d*) occurs downstream of the impinging oblique shock. These are typical features of SBLI flows, consistent with the results in previous numerical studies (Pirozzoli & Grasso 2006; Pirozzoli & Bernardini 2011*a*; Volpiani *et al.* 2018).

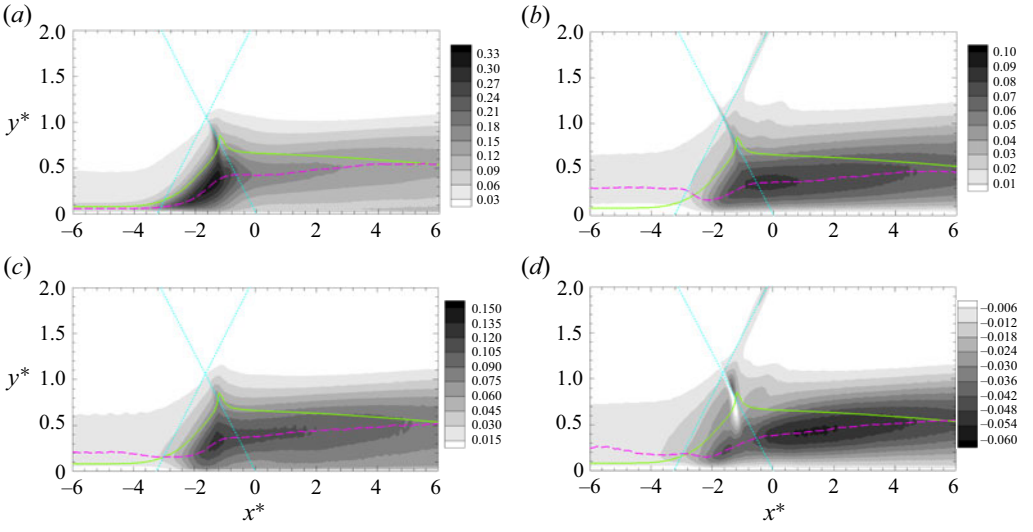

Figure 5. Reynolds stress near the interaction zone, normalized by $\rho_\infty U_\infty^2$, for (*a*) R_{uu}, (*b*) R_{vv}, (*c*) R_{ww}, and (*d*) R_{uv}. Magenta dashed lines indicate the locations of the peak values; light-green solid lines indicate average sonic lines; cyan dotted lines indicate approximate impinging and reflected shocks.

We further report the budget of the TKE ($K = \overline{\rho u_i'' u_i''}/2$) transport equation, cast as (Pirozzoli & Bernardini 2011*a*)

$$\frac{\partial K}{\partial t} = \underbrace{-\frac{\partial \bar{\rho}\tilde{u}_j K}{\partial x_j}}_{C_K} \underbrace{-\bar{\rho}\,\widetilde{u_i'' u_j''}\,\frac{\partial \tilde{u}_i}{\partial x_j}}_{P_K} + \underbrace{\frac{\partial}{\partial x_j}\left[-\frac{1}{2}\bar{\rho}\,\widetilde{u_i'' u_i'' u_j''} - \overline{p' u_j''} + \overline{\tau_{ij}' u_i''}\right]}_{D_K}$$
$$\underbrace{-\overline{\tau_{ij}'\frac{\partial u_i''}{\partial x_j}}}_{\varepsilon_K} \underbrace{+\overline{p'\frac{\partial u_i''}{\partial x_i}}}_{\Pi_K} + \underbrace{\overline{u_i''}\left(\frac{\partial \bar{\tau}_{ij}}{\partial x_j} - \frac{\partial \bar{p}}{\partial x_i}\right)}_{B_K}. \tag{4.1}$$

The TKE transport is balanced by the right-hand side of the equation, representing the energy transfer by the mean flow convection C_K, production P_K, diffusion D_K by turbulence, pressure (p') and viscous stress (τ_{ij}') fluctuations, viscous dissipation ε_K, pressure-dilatation Π_k, and mass-diffusion B_K, the last two of which are caused by the genuine compressibility effects.

In figure 6(*a*), we present the contour of the production P_K and the wall-normal distribution of all transport terms at seven streamwise stations across the interaction zone. The average sonic line and the TKE peak location along the streamwise (x) direction are also displayed for comparison. Within the interaction zone, the production term P_K is amplified gradually, and its trend is similar to the amplification of R_{uu} in figure 5(*a*). Its peak location aligns approximately with the average sonic line. The distribution of the budget terms at $x^* = -3.28$ generally resembles that of the canonical compressible wall-bounded turbulence (e.g. Duan, Beekman & Martin 2011), except that the convection term C_K is non-zero, indicating the non-negligible influence of the upstream-travelling sonic waves (Pirozzoli & Grasso 2006). As it approaches downstream, the TKE transport is strongly modified by the impinging shock, where all the budget terms in the TKE transport

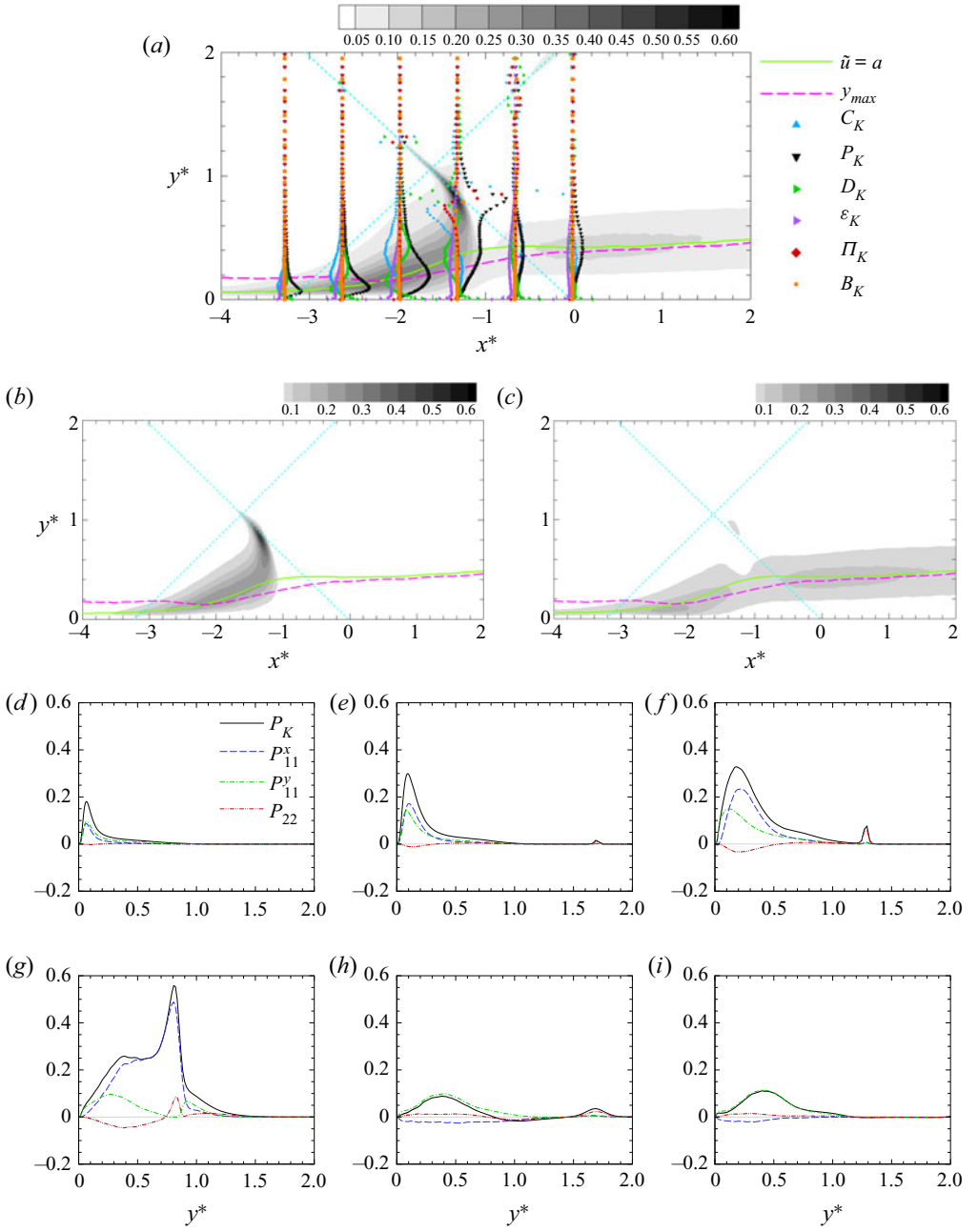

Figure 6. Budget of the TKE transport equation, flooded by: (*a*) P_K, (*b*) P_{11}^x, (*c*) P_{11}^y. Lines indicate: average sonic line (light green solid), maximal TKE location (magenta dashed), approximate impinging and reflected shocks (light blue dotted). Budget at: (*d*) $x^* = -3.28$, (*e*) $x^* = -2.62$, (*f*) $x^* = -1.97$, (*g*) $x^* = -1.32$, (*h*) $x^* = -0.66$, and (*i*) $x^* = 0.0$.

equation are significant, except the Π_k and B_K terms. The Π_k and B_K terms, caused by genuine compressibility effects, manifest their significance only near the strong impinging shock wave, while their participation in TKE energy transfer in other regions is marginal (Jammalamadaka *et al.* 2014). At the end of the interaction zone ($x^* = -0.66$ and 0), the

TKE transport terms are significant merely at $y^* = 0.4$, while the near-wall turbulence is not yet recovered. From the perspective of dynamic process, we can conclude from the budget terms that the TKE is generated by the production term P_K, convected/diffused spatially by C_K and D_K, and mass-diffused or transferred to internal energy by B_K, Π_k and ε_K.

Most early-year studies attributed the turbulence amplification to the vortex-shedding of the separated flow and shear layer. The studies by Humble *et al.* (2007) and Fang *et al.* (2020) proposed a novel mechanism. By splitting the production term P_K as

$$P_K = -\bar{\rho}\,\widetilde{u_i'' u_j''}\,\frac{\partial \tilde{u}_i}{\partial x_j} = -\underbrace{\bar{\rho}\,\widetilde{u''u''}\,\frac{\partial \tilde{u}}{\partial x}}_{P_{11}^x} - \underbrace{\bar{\rho}\,\widetilde{u''v''}\,\frac{\partial \tilde{u}}{\partial y}}_{P_{11}^y} - \underbrace{\bar{\rho}\,\widetilde{u''v''}\,\frac{\partial \tilde{v}}{\partial x}}_{P_{22}^x} - \underbrace{\bar{\rho}\,\widetilde{v''v''}\,\frac{\partial \tilde{v}}{\partial y}}_{P_{22}^y}, \tag{4.2}$$

the terms P_{11}^x and P_{22}^y are regarded as the TKE production by mean flow deceleration, and P_{11}^y and P_{22}^x as by shear. It was pointed out that P_{11}^x is first increased, leading to the amplification of TKE, and conversely resulting in the increment of P_{11}^x, forming a positive feedback loop until the end of the interaction zone.

The physical processes reflected in the present TKE production generally agree with the above elucidation. The distributions of TKE production due to mean flow deceleration P_{11}^x and shear layer P_{11}^y are presented in figures 6(*b*,*c*). The increment of P_{11}^x occurs even upstream of the interaction zone. At $x^* = -3.28$, P_{11}^x is increased to a level same as P_{11}^y. As it approaches downstream across the interaction zone, the P_{11}^x term becomes more prominent than P_{11}^y above $y^* = 0.2$. At the end of the interaction zone, the production term P_K is again dominated by P_{11}^y. The production of R_{vv}, i.e. $P_{22} = P_{22}^x + P_{22}^y$, on the other hand, is much lower than P_{11}^x and P_{11}^y. In general, the present results are consistent with those reported by Humble *et al.* (2007) and Fang *et al.* (2020): the turbulence amplification is first caused by the mean flow deceleration, then the shear layer when it is well-developed.

In this section, we have provided an observation on the evolution of coherent structures across the interaction zone and analysed the budget of TKE transport. The results in the present study are congruous with previous research. In the subsequent discussions, we further inspect the scale-by-scale TKE transport utilizing the budget of TKE spectra transport equation and by so doing relate the emergence of large-scale motions to the turbulence amplification.

5. Spectra of TKE

The premultiplied spanwise energy spectra distributions along the x and y directions near the interaction zone are presented in figure 7 by isosurfaces, along with the spectra distribution at the spanwise scale $\lambda_z^* = 1$ to identify the large-scale motions, and the streamwise locations $x^* = -3.6$, -2.4, -1.2 and 0.0 displayed by contour lines to present the streamwise evolution. The premultiplied spectra of TKE, i.e. $k_z\hat{Q}_{kk}$, are shown in figure 7(*a*). Upstream of the interaction zone, the most energetic motions are prominent only in the near-wall region at $\lambda_z^* \approx 0.5$, i.e. $\lambda_z^+ \approx 100$, corresponding to the characteristic length scale of velocity streaks in canonical wall-bounded turbulence (Pirozzoli & Bernardini 2011*a*). As it enters the interaction zone and approaches the impinging shock, the distribution of the spectra gradually widens in both the λ_z^* and y^* directions, indicating that the energetic motions are excited in wider spanwise-scale and wall-normal ranges. Specifically, the extension of the spectra to the spanwise scales greater than $\lambda_z^* = 1.0$ suggests the emergence or amplification of large-scale motions.

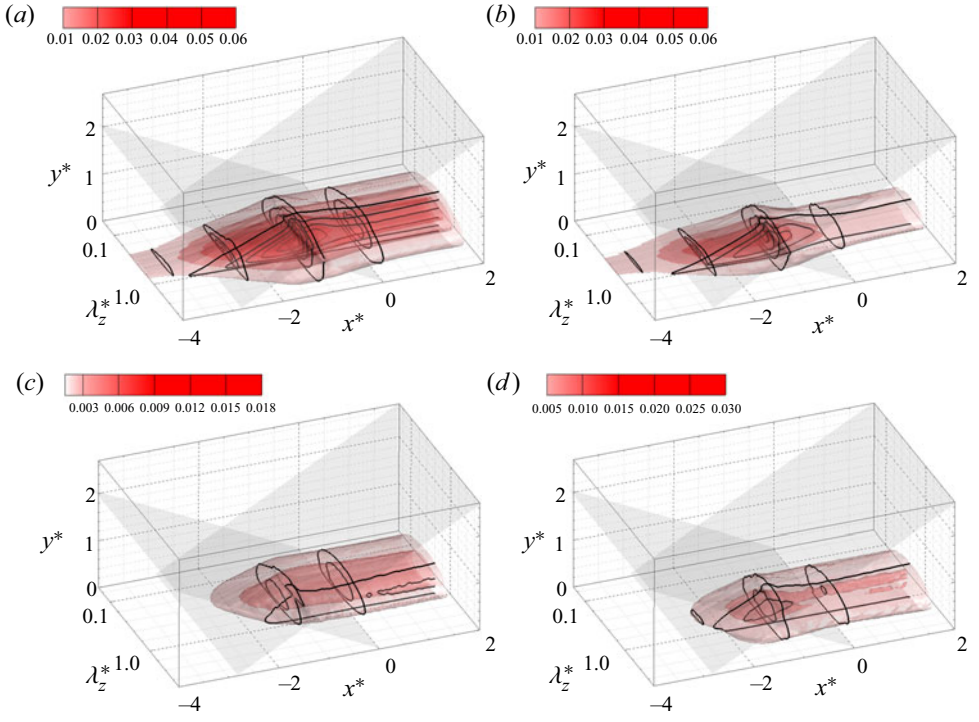

Figure 7. Isosurfaces of the premultiplied spanwise spectra: (*a*) TKE $k_z\hat{Q}_{kk}$; (*b*) streamwise component $k_z\hat{Q}_{11}$; (*c*) wall-normal component $k_z\hat{Q}_{22}$; (*d*) spanwise component $k_z\hat{Q}_{33}$. Contour lines indicate spectra distribution at the spanwise scale of $\lambda_z^* = 1.0$ and the streamwise locations $x^* = -3.6, -2.4, -1.2, 0.0$; grey-shaded planes indicate approximate impinging and reflected shocks.

Inspecting the spectra of the Reynolds normal stresses individually, as displayed in figures 7(*b–d*), we infer that these excited large-scale spectra are attributed primarily to the wall-parallel components $\hat{Q}_{11}$ and $\hat{Q}_{33}$, while the contribution by the wall-normal component $\hat{Q}_{22}$ is less prominent.

We further identify the amplification rate of the spectra, R_Q, defined as

$$R_Q(x^*) = \frac{\max_{y^*,\lambda_z^*} \hat{Q}(x^*, y^*, \lambda_z^*)}{\max_{y^*,\lambda_z^*} \hat{Q}(x_0^*, y^*, \lambda_z^*)}. \tag{5.1}$$

The results are displayed in figure 8(*a*). The spectra peak locations in the wall-normal direction y_R^* and the corresponding spanwise scale $\lambda_{z,R}^*$ are displayed in figures 8(*b*) and 8(*c*), respectively. The amplification of the streamwise component $\hat{Q}_{11}$ is firstly triggered, even upstream of the extrapolated origin of the reflected shock, as shown in figures 8(*a*) and 7(*b*). The $R_{Q_{11}}$ 'overshoots' to a maximal value of 3.5 at $x^* \approx -1.0$ and $y^* \approx 0.4$, where the energetic large- and small-scale motions are both excited. In this process, the most energetic motions are converted from the small-scale motions with $\lambda_{z,R_{11}}^+ \approx 100$ to the large-scale motions with $\lambda_{z,R_{11}}^* \approx 0.9$ (figure 8*c*). At the end of the interaction zone, downstream of $x^* \approx -1.0$, $R_{Q_{11}}$ starts to decay and retains the relatively low value 1.5, while the wall-normal location of the maximum remains at $y^* \approx 0.4$ (figure 8*b*). We can also read from the spectra distribution in figure 7(*b*) that the energetic motions spread widely in scale-space retain for a relatively long streamwise extent, especially for

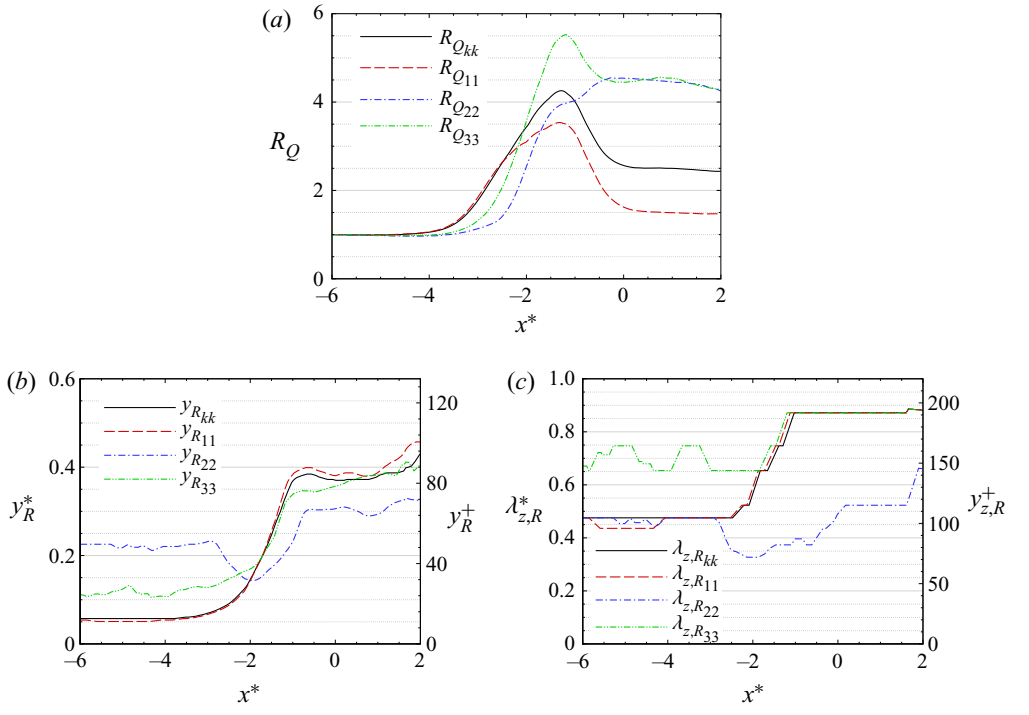

Figure 8. Streamwise distribution of (*a*) amplification rate R_Q, and maximum locations (*b*) y_R^* and (*c*) $\lambda_{z,R}^*$.

those large-scale motions wider than δ_0. For the wall-normal and spanwise components $\hat{Q}_{22}$ and $\hat{Q}_{33}$, the amplification is triggered within the interaction zone, later than $\hat{Q}_{11}$. The maximal amplification rates $R_{Q_{22}}$ and $R_{Q_{33}}$ are attained at $x^* \approx -0.5$ and -1.5, respectively, consistent with the previous observations of R_{ij} in § 4. The $R_{Q_{33}}$ suffers an 'overshooting' to the value 5.5, then returns to 4.5 downstream of the interaction zone, while $R_{Q_{22}}$ increases monotonically and reaches a plateau of 4.5. Downstream of the interaction zone, the maximal spectra density is achieved at $y^* = 0.3$ with the spanwise scale $\lambda_{z,R_{22}}^* \approx 0.45$ for $\hat{Q}_{22}$, and at $y^* = 0.4$ with $\lambda_{z,R_{33}}^* \approx 0.9$ for $\hat{Q}_{33}$. The relations between characteristic scales and wall-normal locations are reminiscent of the streamwise vortices in wall-bounded turbulence (e.g. Hwang & Cossu 2010; Hwang & Bengana 2016).

The above depiction is compatible with the evolution of coherent structures across the impinging shock (recall figure 4). The amplification of $R_{Q_{11}}$, the rise in y_R^* and the increment of $\lambda_{z,R_{11}}^*$ correspond to the formulation of large-scale velocity streaks in the outer region. The latter growth of $R_{Q_{22}}$ and $R_{Q_{33}}$ further suggests that the large-scale cross-stream circulations are formed downstream of the large-scale velocity streaks. With these spatial arrangements, we surmise that the streamwise vortical structures are generated by the twisting of the large-scale velocity streaks, based on the previous investigations on instability/transient growth of velocity streaks (Schoppa & Hussain 2002) in the process of flow transition and the self-sustaining cycle in canonical wall-bounded turbulence (Hwang & Bengana 2016). Related proofs will be provided subsequently.

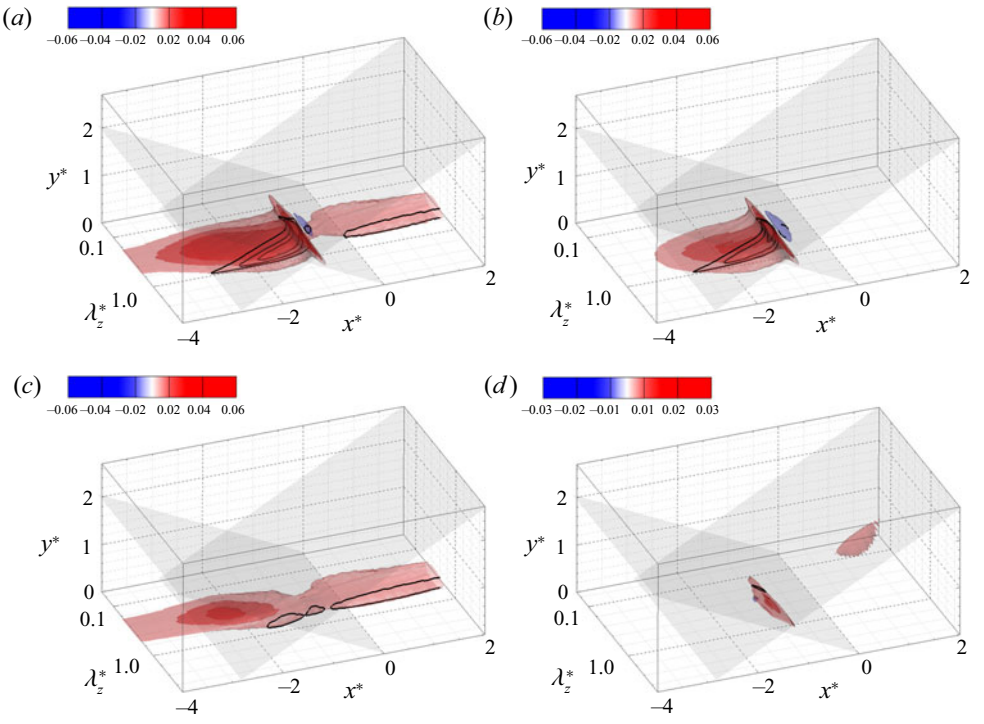

Figure 9. Isosurfaces of the premultiplied spectra of TKE production: (*a*) $k_z\hat{P}_{kk}$, (*b*) $k_z\hat{P}^x_{11}$, (*c*) $k_z\hat{P}^y_{11}$, (*d*) $k_z\hat{P}_{22}$. Contour lines indicate spectra distribution at the spanwise scale of $\lambda^*_z = 1.0$; grey-shaded planes indicate approximate impinging and reflected shocks.

6. Transport of TKE

6.1. *Turbulent production*

Similar to (4.2), the production of TKE spectra transport is split as

$$\hat{P}_{kk} = \hat{P}^x_{11} + \hat{P}^y_{11} + \hat{P}_{22}, \tag{6.1}$$

where

$$\hat{P}^x_{11} = -\frac{1}{2}\hat{Q}_{11}\frac{\partial \tilde{u}}{\partial x}, \tag{6.2}$$

$$\hat{P}^y_{11} = -\frac{1}{2}\hat{Q}_{12}\frac{\partial \tilde{u}}{\partial y}, \tag{6.3}$$

$$\hat{P}_{22} = -\frac{1}{2}\hat{Q}_{21}\frac{\partial \tilde{v}}{\partial x} - \frac{1}{2}\hat{Q}_{22}\frac{\partial \tilde{v}}{\partial y}, \tag{6.4}$$

are the production of $\hat{Q}_{11}$ by mean flow deceleration and shear, and that of $\hat{Q}_{22}$, respectively. The spectra distributions of these production terms are presented in figure 9 by isosurfaces. The total TKE production $\hat{P}_{kk}$ is amplified and spread to wider extents in wall-normal directions and spanwise scales (see figure 9*a*) within the interaction zone, similar to the evolution of TKE spectra (figure 7). As for the decomposed components, $\hat{P}^x_{11}$ in figure 9(*b*) is prominent merely within the interaction zone and constitutes substantially to $\hat{P}_{KK}$ for large-scale motions with $\lambda^*_z \gtrsim 1.0$. The $\hat{P}^y_{11}$ component is first amplified then

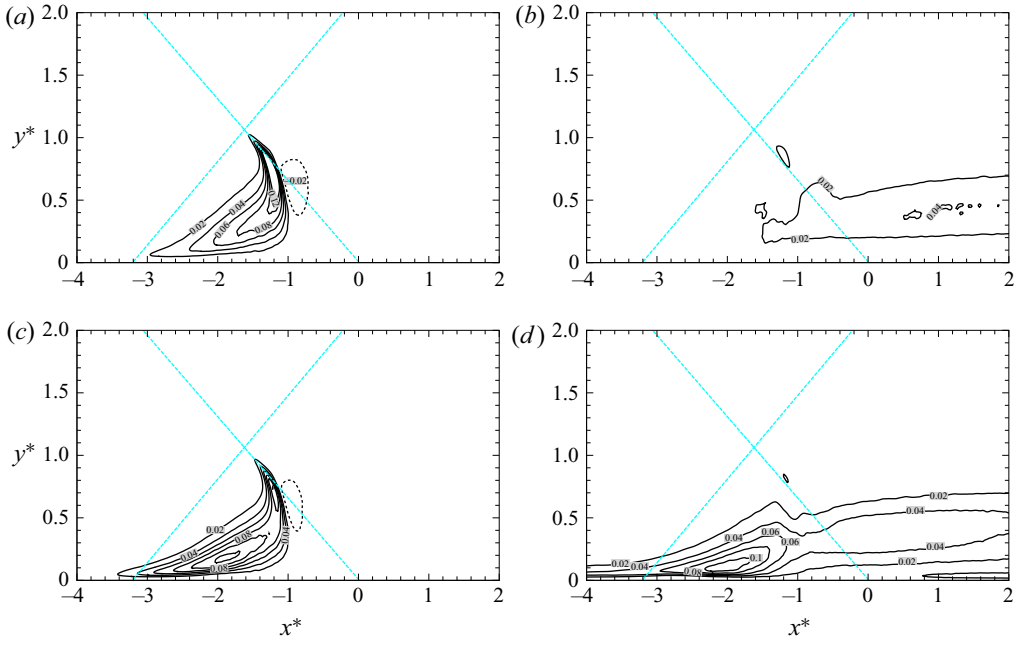

Figure 10. Premultiplied spectra of the decomposed TKE production at (*a*,*b*) $\lambda_z^* = 1.0$ and (*c*,*d*) $\lambda_z^+ = 100$, for (*a*,*c*) $k_z\hat{P}_{11}^x$ and (*b*,*d*) $k_z\hat{P}_{11}^y$. Cyan lines indicate approximate impinging and reflected shocks.

diminished and returns to a moderate value, further dominating the turbulent production downstream. It is significant only at small scale with $\lambda_z^* \lesssim 1.0$. The $\hat{P}_{22}$ component in figure 9(*d*) is trivial except near the shocks.

Considering their significance, the spectra $\hat{P}_{11}^x$ and $\hat{P}_{11}^y$ at the characteristic large and small scales, i.e. $\lambda_z^* \approx 1.0$ and $\lambda_z^+ \approx 100$, are presented further in figure 10. For the production at the large-scale $\lambda_z^* \approx 1.0$, as shown in figures 10(*a*,*b*), the $\hat{P}_{11}^x$ component is dominant within the interaction zone. Its amplification starts to evidence at $x^* \approx -3.0$, increases rapidly, and then drops to a negligible value at $x^* \approx -1.0$. A small region of negative production is observed across the nominal impinging shock, due to the acceleration of the mean flow. The $\hat{P}_{11}^y$ component, on the other hand, manifests itself only at the end of the interaction zone $x^* \approx -1.0$, where the shear layer is fully developed. In the post-shock region, $\hat{P}_{11}^y$ remains at the relatively low level 0.02, indicating its weak contribution to the production of large-scale motions downstream of the interaction zone. As for the production at the small-scale $\lambda_z^+ \approx 100$, as shown in figures 10(*c*,*d*), the $\hat{P}_{11}^x$ and $\hat{P}_{11}^y$ components are equivalently significant. They start to increase simultaneously at $x^* \approx -3.5$, and attain local maxima at $x^* \approx -2.0$. At the end of the interaction zone, the $\hat{P}_{11}^x$ component decays rapidly to zero, while $\hat{P}_{11}^y$ first decreases and then retains the value 0.04. Notably, a second peak in the near-wall region arises at $x \approx 1.0$, indicating the reformulation of near-wall small-scale structures.

As we discussed previously, the amplification of turbulence should be attributed to first the mean flow deceleration, and then the shear layer once it is well-developed (Humble *et al.* 2007; Fang *et al.* 2020). Although the decomposed production term of TKE transport reported in § 4 generally agrees with this depiction, the present spectral analysis provides

a more detailed yet slightly different interpretation. Specifically, the amplification of large-scale spectral intensity is attributed only to mean-flow deceleration, immediately as it enters the interaction zone, while for the small-scale motions, both the mean-flow deceleration and shear are prominent and increase synchronously within the interaction zone. This should probably be ascribed to the low Reynolds number considered in the present study. According to the definition of these terms in (6.2) and (6.3), the TKE production related to the mean shear should be much more prominent than that by the flow deceleration only when $\partial\tilde{u}/\partial x$ is much smaller than $\partial\tilde{u}/\partial y$, at least by one decade, considering that the variance of u'' is approximately 8–10 times the magnitude of the Reynolds shear stress. Such a circumstance could occur only when the Reynolds number is sufficiently high. Nevertheless, the preceding observation in § 4 and by Fang *et al.* (2020) that the increase of P_{11}^{x} occurs upstream of that of P_{11}^{y} is an integral effect, instead of a scale-by-scale phenomenon.

In the aspect of coherent structures, we ascribe directly the genesis of the large-scale velocity streaks to the mean flow deceleration, which can be related further to the mean adverse pressure gradient (APG) (Babinsky & Harvey 2011, § 2.6). Rose & Childs (1974) suggested that the amplification of the Reynolds stress is similar to that in the incompressible turbulent boundary layers (ITBLs) under APG. Latter studies have revealed further with the energy spectra that turbulence amplification in the outer region in ITBLs under uniform APG is due to the emergence of large-scale motions (Harun *et al.* 2013; Kitsios *et al.* 2017; Yoon, Hwang & Sung 2018; Yoon *et al.* 2020). In supersonic flows, Wang *et al.* (2019*a*,*b*) observed similar and more evident large-scale motions under APG generated by either the small-angle concave walls or external successive compression waves. Wu, Liang & Zhao (2019) linked the large-scale motions to the energy spectra peak in the outer region, further validating the resemblance between compressible and ITBLs under APG. These commonalities lead to an inference that the emergence of the large-scale motions in the present OSBLI flow should be attributed to the APG within the interaction zone.

The spectra of the TKE production merely suggest the formation of large-scale velocity streaks constituted by u''. The large-scale cross-stream circulations constituted by v'' and w'' should be stemmed from the inter-component energy transfer, considering the insignificant $\hat{P}_{22}$ and the inherently zero-valued $\hat{P}_{33}$. This will be demonstrated in the next subsection.

6.2. *Pressure-dilatation and pressure-strain*

The pressure-dilatation term $\hat{\Pi}_{kk}$ exists merely for compressible flows. It transfers energy between kinetic energy and internal energy. Although this term is expected to play a significant role in TKE transfer, at least within the interaction zone, the spectra presented in figure 11(*a*) suggest that genuine compressibility effects are still trivial except near the impinging and reflected shocks. This is consistent with the conclusions in Jammalamadaka *et al.* (2014). A small negative region can be observed at $x^* \approx -1.5$ in the vicinity of the wall, where the genuine compressibility effects are the most obvious for canonical compressible wall-bounded turbulence (Yu, Xu & Pirozzoli 2019, 2020; Yu & Xu 2021).

For the Reynolds normal stresses, the pressure-strain terms $\hat{\Pi}_{11}$, $\hat{\Pi}_{22}$ and $\hat{\Pi}_{33}$ are responsible for the inter-component energy transfer. The results are presented in figures 11(*b–d*). As it goes downstream across the interaction zone, the trend of inter-component TKE transfer is not altered. The TKE is redistributed from u'' and v'' to w'' in the near-wall region, and from u'' to v'' and w'' at higher wall-normal locations.

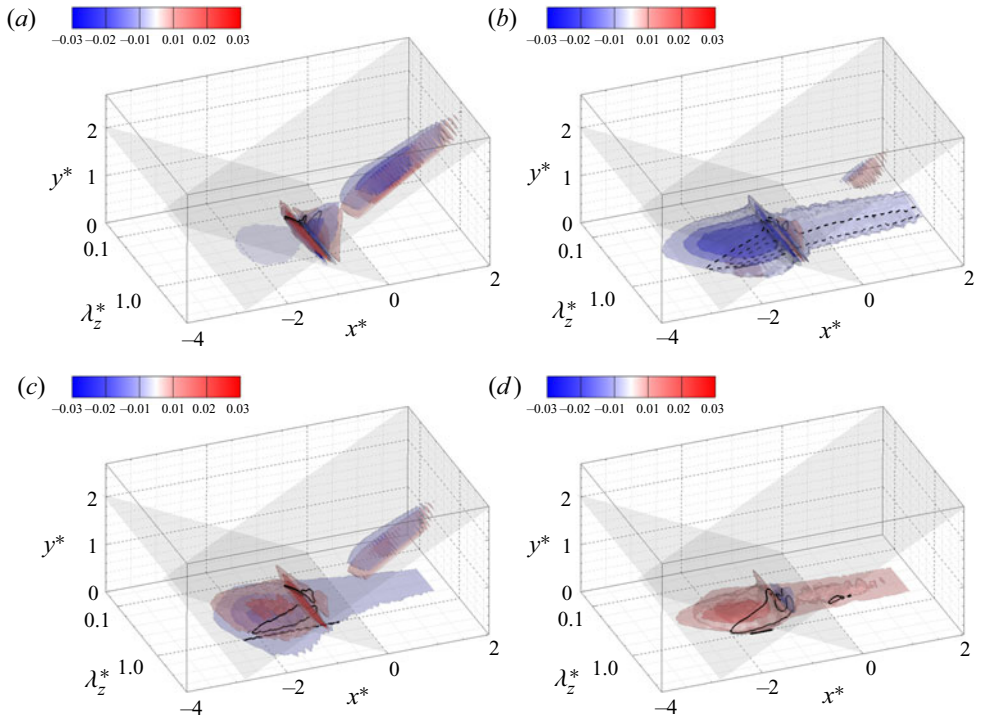

Figure 11. Isosurfaces of the premultiplied spectra of pressure-dilatation and pressure-strain terms: (*a*) $k_z\hat{\Pi}_{kk}$, (*b*) $k_z\hat{\Pi}_{11}$, (*c*) $k_z\hat{\Pi}_{22}$, (*d*) $k_z\hat{\Pi}_{33}$. Contour lines indicate spectra distribution at the spanwise scale of $\lambda_z^* = 1.0$; grey-shaded planes indicate approximate impinging and reflected shocks.

Note that in the post-shock region, the transfer of TKE from u'' to v'' is not strong enough to be manifested by the isosurfaces.

In §§ 5 and 6.1, we observed that the formation of the large-scale velocity streaks occurs upstream of the emergence of the large-scale cross-stream circulations. We also showed that the large-scale velocity streaks are induced by the adverse pressure gradient. The pressure-strain terms considered herein further explain the generation of large-scale cross-stream circulations. Considering that the production terms $\hat{P}_{22}$ and $\hat{P}_{33}$ are either insignificant or zero, we infer that the energetic large-scale cross-stream circulations composed of v'' and w'' emerging at the end of the interaction zone are induced by the inter-component energy transfer from u''.

Intriguingly, in the self-sustaining cycles of wall-bounded turbulence, the instability and/or transient growth leads to the meandering of the velocity streaks (Schoppa & Hussain 2002), and further forming streamwise vortices via vortex stretching and advection (Jiménez 2015). These processes proved to be related to the inter-component energy transfer by pressure-strain terms as well (Cho, Choi & Hwang 2016; Cho *et al.* 2018; Doohan, Willis & Hwang 2021; Kawata & Tsukahara 2021). This resemblance partially substantiates our previous presumption that the large-scale cross-stream circulations are prompted by the instability/transient growth of large-scale velocity streaks.

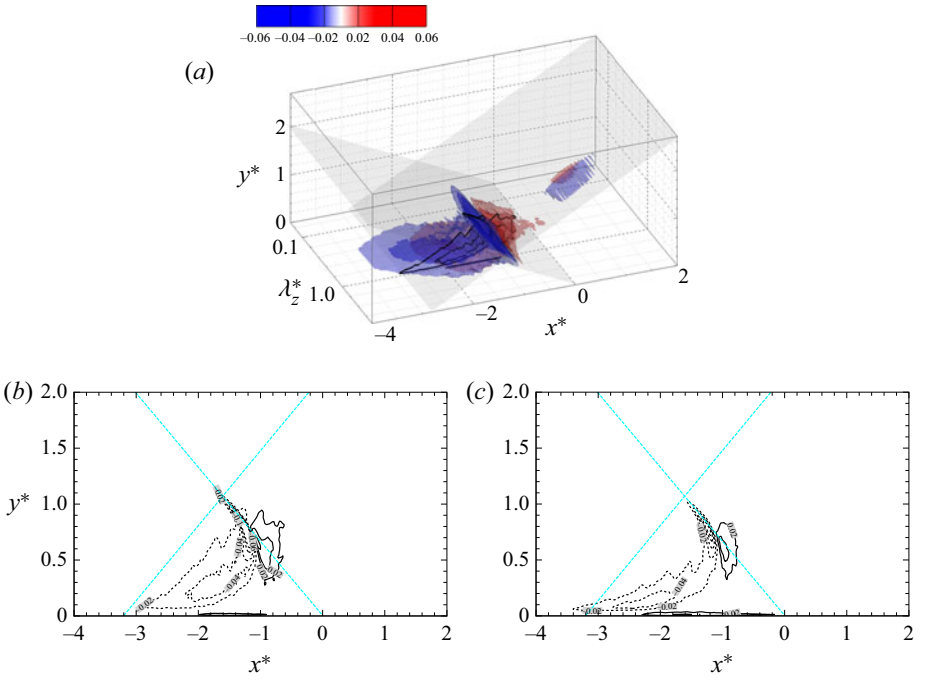

Figure 12. (*a*) Isosurfaces of the premultiplied spectra of TKE spatial transport $k_z(\hat{B}_{kk} + \hat{C}_{kk} + \hat{D}_{kk})$; contour lines indicate spectra at the spanwise scale of $\lambda_z^* = 1.0$; grey-shaded planes indicate impinging and reflected shocks. (*b*,*c*) Spectra distribution at $\lambda_z^* = 1.0$ and $\lambda_z^+ = 100$; cyan lines indicate approximate impinging and reflected shocks.

6.3. *Convection, diffusion and mass-diffusion*

The convection term $\hat{C}_{kk}$ and the diffusion term $\hat{D}_{kk}$ represent the spatial energy transport by mean flow and fluctuations, respectively. The mass-diffusion term comes from the difference between the ensemble and Favre averages of velocity fluctuations. It reflects directly the genuine compressibility effects caused by density fluctuations. Herein, we add these three terms together and regard the summation as the TKE spatial transfer.

The spectra distribution of this budget term is displayed in figure 12(*a*). The contours at the scales $\lambda_z^* = 1.0$ and $\lambda_z^+ = 100$ are displayed in figures 12(*b*) and 12(*c*), respectively. The spatial energy transfer plays a significant role only within the interaction zone. The amplified production term observed in figure 9 is essentially balanced by this term, indicating that the amplified energy is transferred spatially downstream to the post-shock region, or downwards to the near-wall region. This is similar to the TKE budget analysis performed by Li *et al.* (2010) and Tong *et al.* (2017). Notably, inspecting $\hat{B}_{kk}$, $\hat{C}_{kk}$ and $\hat{D}_{kk}$ individually, we find that $\hat{C}_{kk}$ and $\hat{D}_{kk}$ are much stronger than $\hat{B}_{kk}$, indicating that the genuine compressibility effects caused by the density fluctuations are insignificant.

6.4. *Inter-scale energy transfer and dissipation*

The inter-scale energy transfer $\hat{T}_{kk}$ reflects the turbulent energy cascade. As presented in figure 13(*a*), the energy is transferred from large- to small-scale motions, consistent with

the classical energy cascade process depicted by Richardson (Pope 2000). The inverse energy transfer from small- to large-scale motions is not evident. The spectra distributions of $\hat{T}_{kk}$ at $x^* = -4.0, -3.0, -2.0, -1.0$ are presented in figures 13(*c–f*), respectively. Upstream of the interaction zone, the spectra of the inter-scale energy transfer share resemble those in incompressible channel flows (Lee & Moser 2015; Cho *et al.* 2018). The energy is transferred primarily from the scale $\lambda_z^+ \approx 100$ to $\lambda_z^+ \approx 20$. Inverse energy transfer from small- to large-scale motions at $\lambda_z^* \approx 1.0$ is also evident, which has been observed widely in the spanwise spectra of the TKE transport process (Lee & Moser 2015; Auléry *et al.* 2017; Cho *et al.* 2018). As it approaches downstream at $x^* = -3.0$ and -2.0, this budget term is gradually intensified, with the negative peak location remaining at $\lambda_z^+ \approx 100$ in the scale space, and moving outwards in the wall-normal direction. The inverse energy transfer from $\lambda_z^+ \approx 100$ to $\lambda_z^* \gtrsim 1.0$ is still visible. The corresponding local maxima are also moving outwards and to larger scales. At $x^* = -1.0$, where the amplification rate of TKE spectra reaches maxima, there is only energy transfer from large-scale at $\lambda_z^* \approx 1.0$ to smaller-scale motions, while the inverse energy transfer fades away. Although the net inverse energy transfer occurs in the process of turbulence amplification at the start of the interaction zone, its contribution to the genesis of large-scale motions is scanty due to its smallness in comparison with the production term.

As expected, the dissipation term $\hat{\varepsilon}_{kk}$, presented in figure 13(*b*), is significant merely close to the wall and concentrated at small scales.

7. Spanwise uniform oscillations

The preceding discussions focused on the motions with finite spanwise length scales, while the turbulent fluctuations caused by the spanwise-uniform unsteadiness are not involved. In this section, we discuss the energy transfer of these spanwise-uniform turbulent fluctuations.

The energy of spanwise-uniform oscillations (SUOs) is extracted from the Fourier mode at $k_z = 0$. The spectra distribution of TKE in the x–y plane near the interaction zone is presented in figure 14(*a*). The strong SUOs can be classified according to the wall-normal coordinate and their physical counterparts. The strong spectra density above the boundary layer ($y^* \gtrsim 1.0$) corresponds to the unsteady reflected shock wave (Plotkin 1975; Clemens & Narayanaswamy 2014), hereinafter referred to as the 'shock unsteadiness'. That inside the boundary layer ($y^* \lesssim 1.0$) within the interaction zone corresponds to the low-frequency 'breathing' or intermittency of the flow separation (Clemens & Narayanaswamy 2014) and the possibly existing quasi-two-dimensional vortex shedding due to the Kelvin–Helmholtz instability (Dupont *et al.* 2008; Helm *et al.* 2014), hereinafter referred to as the 'inner unsteadiness'. Compared with the finite spanwise length scales motions (FSMs), it is less energetic, with spectra maximum a decade lower. The TKE of SUOs starts to magnify at $x^* \approx -3$, and reaches maximum at $x^* \approx -1.0$ and $y^* \approx 0.4$, downstream of which it gradually decays, similar to FSMs.

The spectra of energy transfer budget terms are shown in figures 14(*b–f*). For the shock unsteadiness, although the budget terms are strong, they are prominent only adjacent to the impinging and reflected shocks. The TKE is produced by the production term, convected/diffused upstream/downstream, and transferred from/to the internal energy by pressure-dilatation correlation. The inter-scale energy transfer for the shock unsteadiness is negative, indicating that the shock unsteadiness is partially responsible for its wrinkling. Although the above scenario seems plausible, we are obliged to stress that

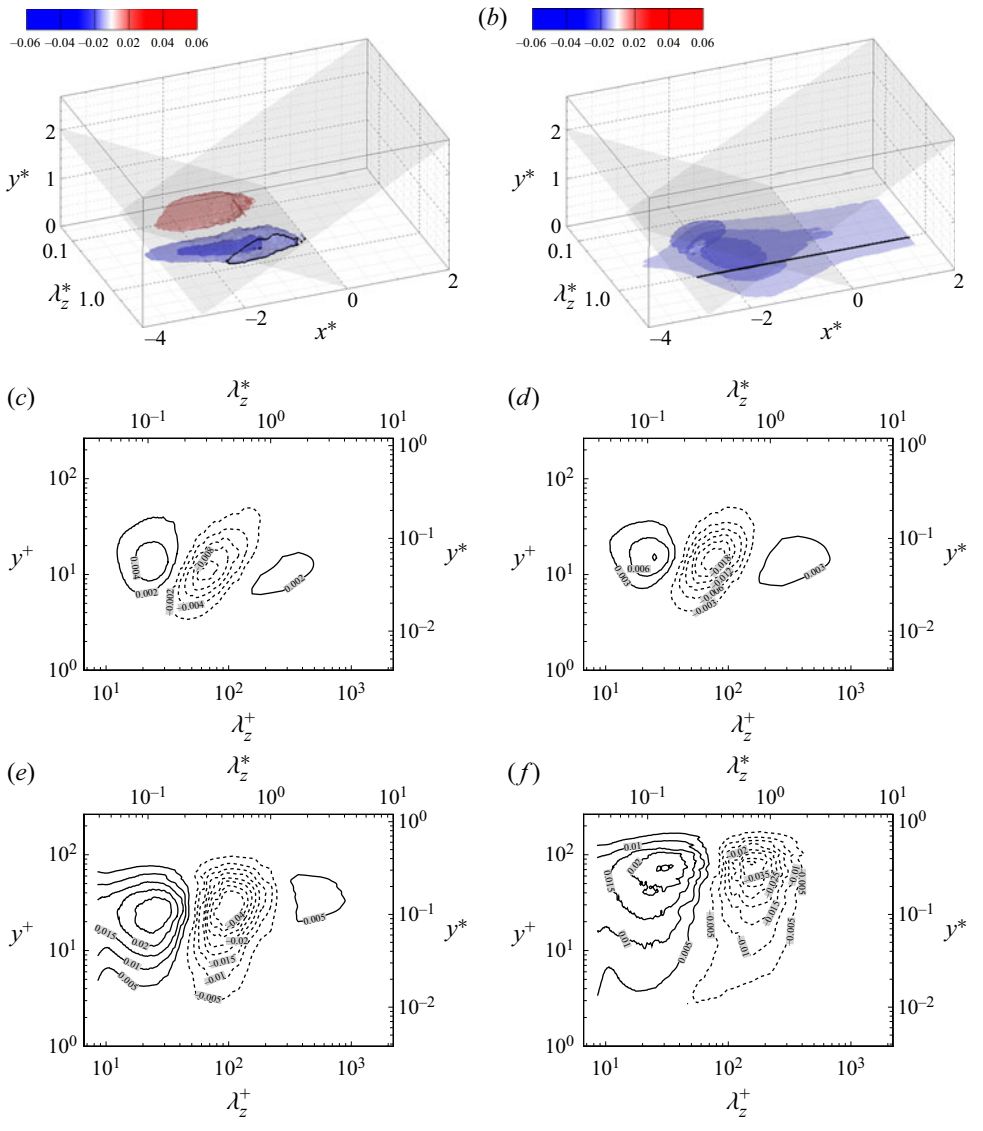

Figure 13. Isosurfaces of the premultiplied spectra of (*a*) inter-scale energy transfer $k_z\hat{T}_{kk}$ and (*b*) dissipation $k_z\hat{\varepsilon}_{kk}$; contour lines indicate spectra at the spanwise scale of $\lambda_z^* = 1.0$; grey-shaded planes indicate approximate impinging and reflected shocks. (*c–f*) The $k_z\hat{T}_{kk}$ distribution at $x^* = -4.0, -3.0, -2.0, -1.0$, respectively.

these interpretations must be made with caution. For numerical stability, high numerical dissipation is applied to resolve the shock wave, which reduces the accuracy of the results, especially in spectral analysis.

As for the inner unsteadiness, the energy transfer is dominated by production $\hat{P}_{kk}$, convection/diffusion/mass-diffusion $\hat{B}_{kk} + \hat{C}_{kk} + \hat{D}_{kk}$, and inter-scale energy transfer $\hat{T}_{kk}$. The dissipation $\hat{\varepsilon}_{kk}$ is significant merely close to the wall. The production term $\hat{P}_{kk}$ manifests itself within the interaction zone from $x^* \approx -3$ to $x^* \approx -1$. It is weaker than the contribution from the inter-scale energy transfer $\hat{T}_{kk}$, which is primarily responsible for the SUO TKE amplification, even downstream of the interaction zone. Its positiveness

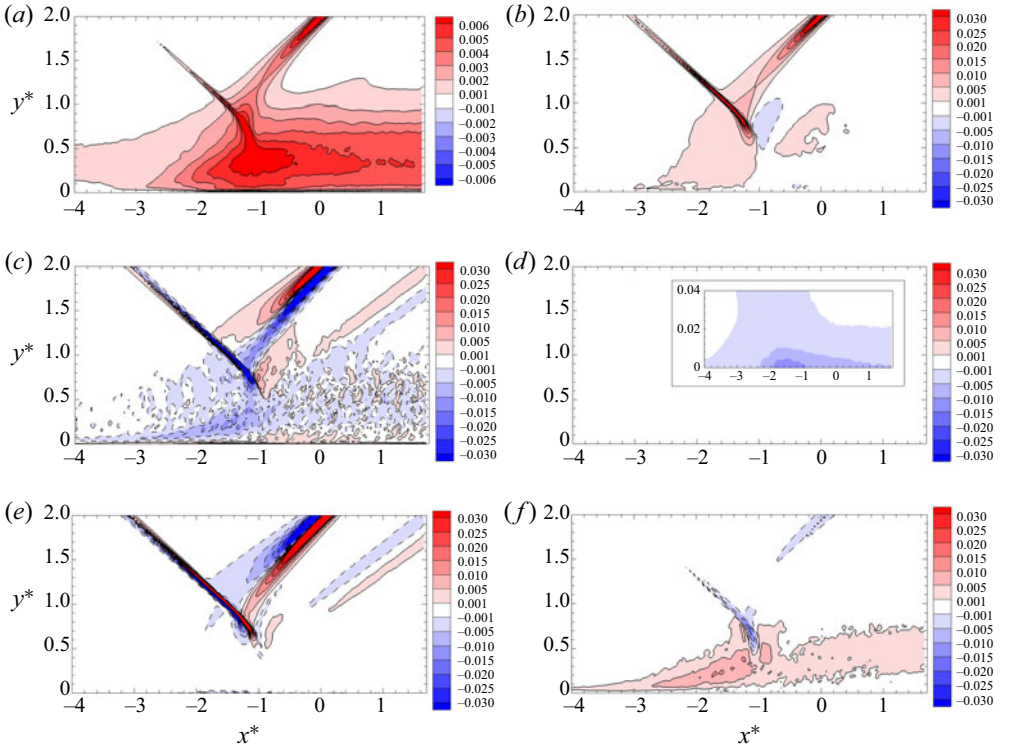

Figure 14. The TKE spectra and the transport budget terms at $k_z = 0$, for (*a*) $\hat{Q}_{kk}$, (*b*) $\hat{P}_{kk}$, (*c*) $\hat{B}_{kk} + \hat{C}_{kk} + \hat{D}_{kk}$, (*d*) $\hat{\varepsilon}_{kk}$, (*e*) $\hat{\Pi}_{kk}$, (*f*) $\hat{T}_{kk}$. The inset in (*d*) is stretched vertically from 0 to 0.04.

indicates that the TKE of SUOs is transferred from FSMs. We can comprehend this process as the global instability induced by small-scale disturbances (Touber & Sandham 2009; Nichols *et al.* 2017; Pasquariello *et al.* 2017).

8. Concluding remarks

Oblique shock wave/turbulent boundary layer interaction is a ubiquitous flow phenomenon in aerospace engineering. In this paper, we present the scale-by-scale inspections of turbulence amplification and the evolution of coherent structures within the interaction zone. To do this, we derived the TKE spectra transport equation. The spectral analysis enhances our comprehension of the association between turbulence amplification and the genesis of large-scale structures.

For the presently considered case, with the free-stream Mach number being 2.28 and the angle of impinging shock wave being 33.2°, the flow goes through a mild separation with a small mean separation bubble in the interaction zone. The TKE budget analysis confirms the preceding conclusion that the turbulence amplification is excited by first mean flow deceleration, and then the shear layer once it is well-developed. The spectra distribution shows that the most energetic motions are converted from the near-wall small-scale motions with $\lambda_z^+ \approx 100$ at $y^+ \approx 15$ to large-scale motions with $\lambda_z^* \approx 0.9$ at $y^* \approx 0.4$, which retain for a long extent downstream. It also suggests that the turbulent amplification is associated directly with the emergence of large-scale motions. Within the interaction zone, the spectra of the TKE production reveal the distinctive

process of turbulence amplification between large-scale and small-scale motions: the former primarily by the mean flow deceleration, while the latter by both the mean flow deceleration and the mean shear. The seemingly first triggered production by mean flow deceleration in TKE budget is an integral effect instead of a scale-by-scale phenomenon for the presently considered low-Reynolds-number case. The production term engenders primarily the energy of streamwise velocity fluctuation, which is redistributed to the other two velocity components by the pressure-strain term. The energy within the interaction zone is transported downstream, transferred to small scales, and dissipated by viscosity. The inverse energy transfer from small scales ($\lambda_z^+ \approx 100$) to large scales ($\lambda_z^* \gtrsim 1.0$) is also observed. However, its contribution is much less prominent compared with the production term. The genuine compressibility effects are negligible, except near the shocks.

The TKE spectra transport analysis also sheds some light on the genesis of large-scale motions within the interaction zone. Based on the commonalities between the presently studied flow and the existing investigations on turbulent boundary layers under adverse pressure gradient, we can elucidate that it is the mean adverse pressure gradient that induces the generation of large-scale velocity streaks. That the pressure-strain term transfers the energy from the streamwise velocity component to other components partially substantiates that the formulation of the cross-stream circulations is probably induced by the modal/non-modal instability of the velocity streaks, based on the scenarios of the self-sustaining cycles in wall-bounded turbulence.

The spanwise uniform motions correspond to the unsteadiness of the reflected shock and the flow separation or vortex shedding. The latter proves to be generated primarily by the inter-scale energy transfer that transports the TKE from finite-scale motions to spanwise uniform motions, possibly due to the global instability of the mean flow.

The present scale-by-scale energy transfer may benefit the improvement of subgrid modelling for large-eddy simulations, which will be considered in our future study.

Funding. This work is supported by the National Key R&D Program of China (grant no. 2019YFA0405201) and the National Natural Science Foundation of China (grant nos 92052301, 12202469).

Declaration of interests. The authors report no conflict of interest.

Author ORCIDs.
Ming Yu https://orcid.org/0000-0001-7772-833X;
XianXu Yuan https://orcid.org/0000-0002-7668-0116;
ChunXiao Xu https://orcid.org/0000-0001-5292-8052.

References

Andreopoulos, Y., Agui, J.H. & Briassulis, G. 2000 Shock wave–turbulence interactions. *Annu. Rev. Fluid Mech.* **32** (1), 309–345.

Anyiwo, J.C. & Bushnell, D.M. 1982 Turbulence amplification in shock-wave boundary-layer interaction. *AIAA J.* **20** (7), 893–899.

Arun, S., Sameen, A., Srinivasan, B. & Girimaji, S. 2021 Scale-space energy density function transport equation for compressible inhomogeneous turbulent flows. *J. Fluid Mech.* **920**, A31.

Auléry, F., Dupuy, D., Toutant, A., Bataille, F. & Zhou, Y. 2017 Spectral analysis of turbulence in anisothermal channel flows. *Comput. Fluids* **151**, 115–131.

Auléry, F., Toutant, A., Bataille, F. & Zhou, Y. 2015 Energy transfer process of anisothermal wall-bounded flows. *Phys. Lett.* A **379** (24–25), 1520–1526.

Babinsky, H. & Harvey, J.K. 2011 *Shock Wave–Boundary-Layer Interactions*. Cambridge Aerospace Series, vol. 32. Cambridge University Press.

Baidya, R., Scharnowski, S., Bross, M. & Kähler, C.J. 2020 Interactions between a shock and turbulent features in a Mach 2 compressible boundary layer. *J. Fluid Mech.* **893**, A15.

BERNARDINI, M., ASPROULIAS, I., LARSSON, J., PIROZZOLI, S. & GRASSO, F. 2016 Heat transfer and wall temperature effects in shock wave turbulent boundary layer interactions. *Phys. Rev. Fluids* **1** (8), 084403.

BERNARDINI, M., MODESTI, D., SALVADORE, F. & PIROZZOLI, S. 2021 STREAmS: a high-fidelity accelerated solver for direct numerical simulation of compressible turbulent flows. *Comput. Phys. Commun.* **263**, 107906.

BERNARDINI, M., PIROZZOLI, S. & GRASSO, F. 2011 The wall pressure signature of transonic shock/boundary layer interaction. *J. Fluid Mech.* **671**, 288–312.

CHO, M., CHOI, H. & HWANG, Y. 2016 On the structure of pressure fluctuations of self-sustaining attached eddies. In *APS Division of Fluid Dynamics Meeting Abstracts*, pp. A33–003.

CHO, M., HWANG, Y. & CHOI, H. 2018 Scale interactions and spectral energy transfer in turbulent channel flow. *J. Fluid Mech.* **854**, 474–504.

CLEMENS, N. & NARAYANASWAMY, V. 2014 Low-frequency unsteadiness of shock wave/turbulent boundary layer interactions. *Annu. Rev. Fluid Mech.* **46**, 469–492.

DÉLERY, J., MARVIN, J.G. & RESHOTKO, E. 1986 Shock-wave boundary layer interactions. *Tech. Rep.* Advisory Group for Aerospace Research and Development Neuilly-Sur-Seine (France).

DOLLING, D.S. 2001 Fifty years of shock-wave/boundary-layer interaction research: what next? *AIAA J.* **39** (8), 1517–1531.

DOMARADZKI, J.A., LIU, W., HÄRTEL, C. & KLEISER, L. 1994 Energy transfer in numerically simulated wall-bounded turbulent flows. *Phys. Fluids* **6** (4), 1583–1599.

DOOHAN, P., WILLIS, A.P. & HWANG, Y. 2021 Minimal multi-scale dynamics of near-wall turbulence. *J. Fluid Mech.* **913**, A8.

DUAN, L., BEEKMAN, I. & MARTIN, M.P. 2011 Direct numerical simulation of hypersonic turbulent boundary layers. Part 3. Effect of Mach number. *J. Fluid Mech.* **672**, 245–267.

DUCROS, F., FERRAND, V., NICOUD, F., WEBER, C., DARRACQ, D., GACHERIEU, C. & POINSOT, T. 1999 Large-eddy simulation of the shock/turbulence interaction. *J. Comput. Phys.* **152** (2), 517–549.

DUPONT, P., HADDAD, C., ARDISSONE, J.P. & DEBIEVE, J.F. 2005 Space and time organisation of a shock wave/turbulent boundary layer interaction. *Aerosp. Sci. Technol.* **9** (7), 561–572.

DUPONT, P., HADDAD, C. & DEBIEVE, J.F. 2006 Space and time organization in a shock-induced separated boundary layer. *J. Fluid Mech.* **559**, 255–277.

DUPONT, P., PIPONNIAU, S. & DUSSAUGE, J.P. 2019 Compressible mixing layer in shock-induced separation. *J. Fluid Mech.* **863**, 620–643.

DUPONT, P., PIPONNIAU, S., SIDORENKO, A. & DEBIÈVE, J.F. 2008 Investigation by particle image velocimetry measurements of oblique shock reflection with separation. *AIAA J.* **46** (6), 1365–1370.

DUPUY, D., TOUTANT, A. & BATAILLE, F. 2018*a* Equations of energy exchanges in variable density turbulent flows. *Phys. Lett.* A **382** (5), 327–333.

DUPUY, D., TOUTANT, A. & BATAILLE, F. 2018*b* Turbulence kinetic energy exchanges in flows with highly variable fluid properties. *J. Fluid Mech.* **834**, 5–54.

FANG, J., ZHELTOVODOV, A.A., YAO, Y., MOULINEC, C. & EMERSON, D. 2020 On the turbulence amplification in shock-wave/turbulent boundary layer interaction. *J. Fluid Mech.* **897**, A32.

HAMBA, F. 2019 Inverse energy cascade and vortical structure in the near-wall region of turbulent channel flow. *Phys. Rev. Fluids* **4** (11), 114609.

HARUN, Z., MONTY, J.P., MATHIS, R. & MARUSIC, I. 2013 Pressure gradient effects on the large-scale structure of turbulent boundary layers. *J. Fluid Mech.* **715**, 477–498.

HELM, C., MARTIN, M.P. & DUPONT, P. 2014 Characterization of the shear layer in a Mach 3 shock/turbulent boundary layer interaction. *J. Phys.: Conf. Ser.* **506**, 012013.

HUMBLE, R.A., SCARANO, F. & VAN OUDHEUSDEN, B.W. 2007 Particle image velocimetry measurements of a shock wave/turbulent boundary layer interaction. *Exp. Fluids* **43** (2), 173–183.

HUMBLE, R.A., SCARANO, F. & VAN OUDHEUSDEN, B.W. 2009 Unsteady aspects of an incident shock wave/turbulent boundary layer interaction. *J. Fluid Mech.* **635**, 47–74.

HWANG, Y. & BENGANA, Y. 2016 Self-sustaining process of minimal attached eddies in turbulent channel flow. *J. Fluid Mech.* **795**, 708–738.

HWANG, Y. & COSSU, C. 2010 Self-sustained process at large scales in turbulent channel flow. *Phys. Rev. Lett.* **105** (4), 044505.

JAMMALAMADAKA, A., LI, Z. & JABERI, F. 2014 Numerical investigations of shock wave interactions with a supersonic turbulent boundary layer. *Phys. Fluids* **26** (5), 87–108.

JIANG, G.S. & SHU, C.W. 1996 Efficient implementation of weighted ENO schemes. *J. Comput. Phys.* **126** (1), 202–228.

JIMÉNEZ, J. 2015 Direct detection of linearized bursts in turbulence. *Phys. Fluids* **27** (6), 065102.

KAWATA, T. & TSUKAHARA, T. 2021 Scale interactions in turbulent plane Couette flows in minimal domains. *J. Fluid Mech.* **911**, A55.

KITSIOS, V., SEKIMOTO, A., ATKINSON, C., SILLERO, J.A., BORRELL, G., GUNGOR, A.G., JIMÉNEZ, J. & SORIA, J. 2017 Direct numerical simulation of a self-similar adverse pressure gradient turbulent boundary layer at the verge of separation. *J. Fluid Mech.* **829**, 392–419.

KLEIN, M., SADIKI, A. & JANICKA, J. 2003 A digital filter based generation of inflow data for spatially developing direct numerical or large eddy simulations. *J. Comput. Phys.* **186** (2), 652–665.

LEE, M. & MOSER, R.D. 2015 Spectral analysis on Reynolds stress transport equation in high Re wall-bounded turbulence. In *International Symposium on Turbulence and Shear Flow Phenomena (TSFP-9)*.

LEE, M. & MOSER, R.D. 2019 Spectral analysis of the budget equation in turbulent channel flows at high Reynolds number. *J. Fluid Mech.* **860**, 886–938.

LI, X.L., FU, D.X., MA, Y.W. & LIANG, X. 2010 Direct numerical simulation of shock/turbulent boundary layer interaction in a supersonic compression ramp. *Sci. China Phys. Mech. Astron.* **53** (9), 1651–1658.

LIGRANI, P.M., MCNABB, E.S., COLLOPY, H., ANDERSON, M. & MARKO, S.M. 2020 Recent investigations of shock wave effects and interactions. *Adv. Aerodyn.* **2** (1), 4.

LIU, S.H., CHENG, Z.Q., JIANG, Y., LU, J.F., ZHANG, M.P. & ZHANG, S.H. 2022 Numerical simulation of a complex moving rigid body under the impingement of a shock wave in 3D. *Adv. Aerodyn.* **4** (1), 8.

LOGINOV, M.S., ADAMS, N.A. & ZHELTOVDOV, A.A. 2006 Large-eddy simulation of shock-wave/turbulent-boundary-layer interaction. *J. Fluid Mech.* **565**, 135–169.

LUMLEY, J.L. 1964 Spectral energy budget in wall turbulence. *Phys. Fluids* **7** (2), 190–196.

MIZUNO, Y. 2016 Spectra of energy transport in turbulent channel flows for moderate Reynolds numbers. *J. Fluid Mech.* **805**, 171–187.

MUSKER, A.J. 1979 Explicit expression for the smooth wall velocity distribution in a turbulent boundary layer. *AIAA J.* **17** (6), 655–657.

NICHOLS, J.W., LARSSON, J., BERNARDINI, M. & PIROZZOLI, S. 2017 Stability and modal analysis of shock/boundary layer interactions. *Theor. Comput. Fluid Dyn.* **31** (1), 33–50.

PASQUARIELLO, V., HICKEL, S. & ADAMS, N.A. 2017 Unsteady effects of strong shock-wave/boundary-layer interaction at high Reynolds number. *J. Fluid Mech.* **823**, 617–657.

PIROZZOLI, S. 2010 Generalized conservative approximations of split convective derivative operators. *J. Comput. Phys.* **229** (19), 7180–7190.

PIROZZOLI, S. & BERNARDINI, M. 2011*a* Direct numerical simulation database for impinging shock wave/turbulent boundary-layer interaction. *AIAA J.* **49** (6), 1307–1312.

PIROZZOLI, S. & BERNARDINI, M. 2011*b* Turbulence in supersonic boundary layers at moderate Reynolds number. *J. Fluid Mech.* **688**, 120–168.

PIROZZOLI, S., BERNARDINI, M. & GRASSO, F. 2010 Direct numerical simulation of transonic shock/boundary layer interaction under conditions of incipient separation. *J. Fluid Mech.* **657**, 361–393.

PIROZZOLI, S. & COLONIUS, T. 2013 Generalized characteristic relaxation boundary conditions for unsteady compressible flow simulations. *J. Comput. Phys.* **248**, 109–126.

PIROZZOLI, S. & GRASSO, F. 2006 Direct numerical simulation of impinging shock wave/turbulent boundary layer interaction at $M = 2.25$. *Phys. Fluids* **18** (6), 065113.

PLOTKIN, K.J. 1975 Shock wave oscillation driven by turbulent boundary-layer fluctuations. *AIAA J.* **13** (8), 1036–1040.

POPE, S.B. 2000 *Turbulent Flows*, 1st edn. Cambridge University Press.

PRIEBE, S., WU, M. & MARTIN, M.P. 2009 Direct numerical simulation of a reflected-shock-wave/turbulent-boundary-layer interaction. *AIAA J.* **47** (5), 1173–1185.

ROSE, W.C. & CHILDS, M.E. 1974 Reynolds-shear-stress measurements in a compressible boundary layer within a shock-wave-induced adverse pressure gradient. *J. Fluid Mech.* **65** (1), 177–188.

SARIC, W.S. 1994 Görtler vortices. *Annu. Rev. Fluid Mech.* **26** (1), 379–409.

SCHOPPA, W. & HUSSAIN, F. 2002 Coherent structure generation in near-wall turbulence. *J. Fluid Mech.* **453**, 57–108.

SELIG, M.S., ANDREOPOULOS, J., MUCK, K.C., DUSSAUGE, J.P. & SMITS, A.J. 1989 Turbulence structure in a shock wave/turbulent boundary-layer interaction. *AIAA J.* **27** (7), 862–869.

SMITS, A.J. & MUCK, K.C. 1987 Experimental study of three shock wave/turbulent boundary layer interactions. *J. Fluid Mech.* **182**, 291–314.

TONG, F.L., YU, C.P., TANG, Z.G. & LI, X.L. 2017 Numerical studies of shock wave interactions with a supersonic turbulent boundary layer in compression corner: turning angle effects. *Comput. Fluids* **149**, 56–69.

TOUBER, E. & SANDHAM, N. 2009 Large-eddy simulation of low-frequency unsteadiness in a turbulent shock-induced separation bubble. *Theor. Comput. Fluid Dyn.* **23** (2), 79–107.

VOLPIANI, P.S., BERNARDINI, M. & LARSSON, J. 2018 Effects of a nonadiabatic wall on supersonic shock/boundary-layer interactions. *Phys. Rev. Fluids* **3** (8), 083401.

VOLPIANI, P.S., BERNARDINI, M. & LARSSON, J. 2020 Effects of a nonadiabatic wall on hypersonic shock/boundary-layer interactions. *Phys. Rev. Fluids* **5** (1), 014602.

WANG, X., WANG, Z., SUN, M., WANG, Q. & HU, Z. 2019*b* Direct numerical simulation of a supersonic turbulent boundary layer subject to adverse pressure gradient induced by external successive compression waves. *AIP Adv.* **9** (8), 085215.

WANG, Q.C., WANG, Z.G., SUN, M.B., YANG, R., ZHAO, Y.X. & HU, Z. 2019*a* The amplification of large-scale motion in a supersonic concave turbulent boundary layer and its impact on the mean and statistical properties. *J. Fluid Mech.* **863**, 454–493.

WRAY, A.A. 1990 Minimal storage time advancement schemes for spectral methods. NASA Ames Research Center, California, Report No. MS Vol. 202.

WU, X., LIANG, J. & ZHAO, Y. 2019 Direct numerical simulation of a supersonic turbulent boundary layer subjected to a concave surface. *Phys. Rev. Fluids* **4** (4), 044602.

WU, M. & MARTIN, M.P. 2007 Direct numerical simulation of supersonic turbulent boundary layer over a compression ramp. *AIAA J.* **45** (4), 879–889.

WU, M. & MARTIN, M.P. 2008 Analysis of shock motion in shockwave and turbulent boundary layer interaction using direct numerical simulation data. *J. Fluid Mech.* **594**, 71–83.

YOON, M., HWANG, J. & SUNG, H.J. 2018 Contribution of large-scale motions to the skin friction in a moderate adverse pressure gradient turbulent boundary layer. *J. Fluid Mech.* **848**, 288–311.

YOON, M., HWANG, J., YANG, J. & SUNG, H.J. 2020 Wall-attached structures of streamwise velocity fluctuations in an adverse-pressure-gradient turbulent boundary layer. *J. Fluid Mech.* **885**, A12.

YU, M. & XU, C.X. 2021 Compressibility effects on hypersonic turbulent channel flow with cold walls. *Phys. Fluids* **33** (7), 075106.

YU, M., XU, C.X. & PIROZZOLI, S. 2019 Genuine compressibility effects in wall-bounded turbulence. *Phys. Rev. Fluids* **4** (12), 123402.

YU, M., XU, C.X. & PIROZZOLI, S. 2020 Compressibility effects on pressure fluctuation in compressible turbulent channel flows. *Phys. Rev. Fluids* **5** (11), 113401.

ZHANG, Y.S., BI, W.T., HUSSAIN, F. & SHE, Z.S. 2014 A generalized Reynolds analogy for compressible wall-bounded turbulent flows. *J. Fluid Mech.* **739**, 392–420.

ZHELTOVODOV, A.A., LEBIGA, V.A. & YAKOVLEV, V.N. 1989 Measurement of turbulence characteristics in compressible boundary layers near separation zones. *J. Appl. Mech. Tech. Phys.* **30** (3), 442–447.

ZHUANG, Y., TAN, H.J., LI, X., SHENG, F.J. & ZHANG, Y.C. 2018 Görtler-like vortices in an impinging shock wave/turbulent boundary layer interaction flow. *Phys. Fluids* **30** (6), 061702.

ZUO, F.Y., MEMMOLO, A., HUANG, G.P. & PIROZZOLI, S. 2019 Direct numerical simulation of conical shock wave–turbulent boundary layer interaction. *J. Fluid Mech.* **877**, 167–195.